Journal of Materials Science: Materials in Electronics (2020) 31:3729–3749
https://doi.org/10.1007/s10854-020-02994-8

REVIEW

Metal oxides nanoparticles via sol–gel method: a review on synthesis, characterization and applications

Mritunjaya Parashar[1] · Vivek Kumar Shukla[1] · Ranbir Singh[2]

Received: 25 October 2019 / Accepted: 27 January 2020 / Published online: 13 February 2020

Abstract
Metal oxide nanoparticles (MONPs) have enormous applications such as in optical devices, purification systems, biomedical systems, photocatalysis, photovoltaics etc. In this review, we have explored a stable and efficient synthesis protocol of particularly four MONPs: titanium dioxide (TiO_2), tin oxide (SnO_2), tungsten oxide (WO_3) and zinc oxide (ZnO) for getting desired chemical composition, nanostructure, and surface properties. The selection of an efficient synthesis process is a key factor that significantly influences the efficacy of the MONPs. The chemical synthesis of nanoparticles (NPs) via sol–gel route is an effective method to produce high-quality MONPs in comparison to other physical and chemical methods. Sol–gel synthesis is one of the simple, fastest and economically less expensive method, and has its own advantages like low processing temperature, homogeneity of the produced material and formation of the complex structures or composite materials. We believe that this detailed review will provide an insight into sol–gel synthesis of MONPs along with their characterization and diverse applications.

1 Introduction

Metal oxide nanoparticles (MONPs) exhibit unique physical, chemical, optical and electronic properties with respect to those of their bulk counterparts due to the quantum confinement and more availability of the surface atoms than interior atoms for participating in any reaction. Applications of MONPs depend upon their properties such as surface area, shape, size, stability, crystallinity, anti-corrosiveness, conductivity, and photocatalytic activity etc. [1, 2]. It is highly desirable for the commercialization of MONPs to have good controllable qualities during synthesis. In general, the synthesis methods of MONPs can be divided into two groups: (i) physical methods such as ball milling, sputtering, laser ablation, electrospraying, electron beam evaporation etc. and (ii) chemical methods such as sol–gel method, polyol method, hydrothermal method, co-precipitation method, microemulsion technique, chemical vapor deposition etc. (Fig. 1). Physical methods are based on top to down strategy i.e., the synthesis is started from the bulk counterpart of any material which gets depleted systematically for the generation of the fine nanoparticles (NPs) while the chemical methods are mainly based on bottom to up approach i.e., the assembly of atoms or molecules to form distribution of different sizes of NPs. The main advantage of the chemical methods is that it allows the production of particles with a defined size, dimension, composition and structure, which could be useful for various applications such as catalysis, sensing and in electronic devices. In addition, the synthesis via some chemical methods particularly sol–gel route requires low processing temperature and less energy for carrying out the synthesis which makes this method more economical compared to physical methods [3]. The shape and size of the NPs directly affects their properties [4]. For instance, a study by Haruta et al. [5] suggested the catalytic activity of gold NPs depend on the NP-support contact; they found hemispherical NPs to perform better than the spherical NPs. In a similar study, Tian et al. [6] reported the enhanced catalytic activity of platinum NPs. Xu et al. [7] investigated the oxidation of styrene over cubic, truncated triangular nanoplates, and near-spherical Ag NPs and found the rate of reaction over the nanocube particles to be 14 times higher than over the nanoplates, and four times higher

✉ Vivek Kumar Shukla
vivek@gbu.ac.in

✉ Ranbir Singh
ranbir@dongguk.edu

[1] Department of Applied Physics, Gautam Buddha University, Gautam Budh Nagar, Greater Noida, U.P. 201312, India

[2] Department of Energy and Materials Engineering, Dongguk University, Seoul 04620, South Korea

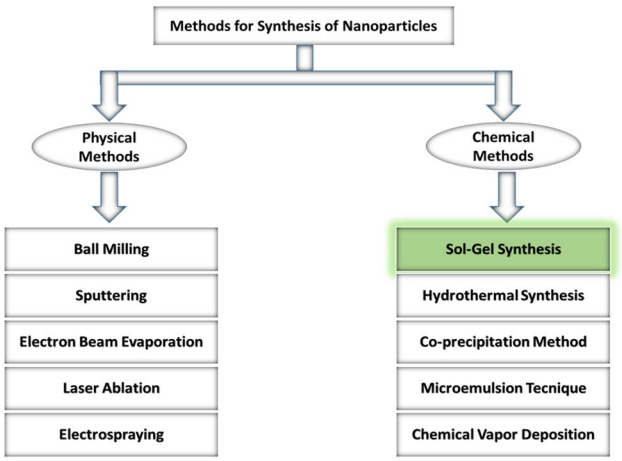

Fig. 1 Different physical and chemical methods used for the synthesis of MONPs

than over the nearly-spherical particles. These studies show the importance of the shape of the synthesized nanostructures and why the shape of the nanostructures during synthesis must be controlled. Thus, a method that can provide better control over shape and size of the NPs is the most suitable for wide range of applications. Different studies in the literature indicate that sol–gel method is one of the promising method to control the shape and size of the NPs [8–10].

In this paper, we reviewed one of the most widely used chemical method i.e., sol–gel method for the synthesis of various MONPs such as TiO_2, ZnO, SnO_2 and WO_3. The processing steps involved in the sol–gel process are discussed in detail. In addition, we have provided a brief discussion about the material characterization to study the crystal structure, optical properties, bandgap, elemental composition, shape, and size. The various applications of MONPs such as in photocatalysis, photovoltaics, sensors, hydrogen production and biomedical areas are discussed in detail.

2 Sol–gel method

Sol–gel method is one of the well-established synthetic approaches to prepare high-quality MONPs as well as mixed oxide composites. This method has excellent control over the texture and surface properties of the materials. In general, sol–gel method can be described in five key steps; hydrolysis, polycondensation, aging, drying and thermal decomposition [11] as described in Fig. 2.

Step 1 Hydrolysis of the precursors such as metal alkoxides takes place in water or alcohols as shown in Fig. 2. For the synthesis of MONPs, oxygen is necessary for the formation of metal oxide which is supplied by water or organic solvents (e.g., alcohols). If water is used as reaction medium, it is known as aqueous sol–gel method; and use of organic solvent as reaction medium for sol–gel process is termed as nonaqueous sol–gel route. In addition to water and alcohol, an acid or a base also helps in the hydrolysis of the precursors. The general chemical reaction for the hydrolysis process is given below:

$$\text{M-OR} + \text{H}_2\text{O} \rightarrow \text{MOH} + \text{ROH} \quad \text{(Hydrolysis)}$$

where M = metal, R = alkyl group (C_nH_{2n+1})

The amount of water strongly influences the gel formation; a higher water content facilitates the formation of a higher ratio of bridging

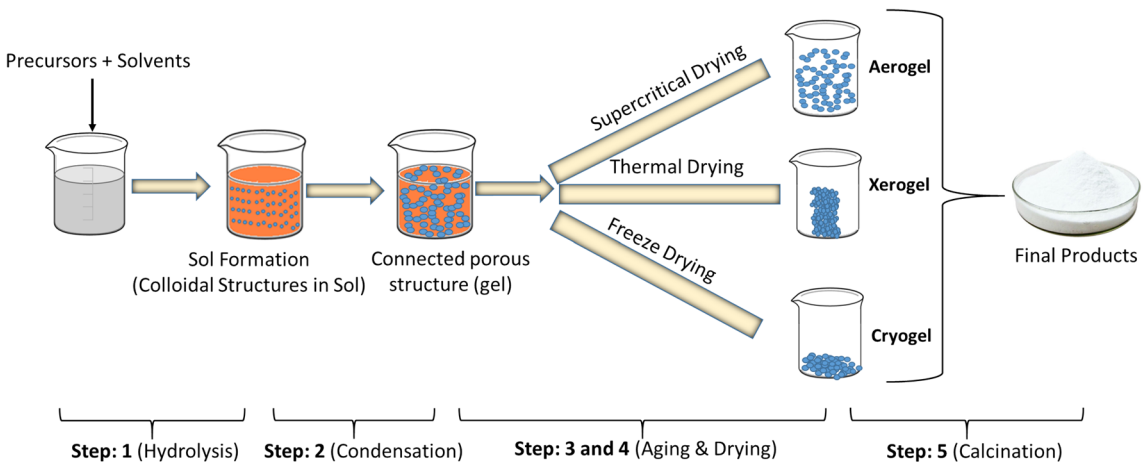

Fig. 2 Steps involved in sol–gel process to synthesize MONPs

to nonbridging oxygens, thus yielding a more polymerized and more branched structure during the condensation [12].

Step 2 This step involves condensation of adjacent molecules, where water/alcohol are eliminated and metal oxide linkages are formed, and polymeric networks grow to colloidal dimensions in the liquid state. Condensation occurs via two processes olation and oxolation. Olation is a process in which hydroxyl (–OH–) bridge is formed between two metal centers (metal–hydroxy-metal bonds) and oxolation is a process in which an oxo (–O–) bridge is formed between two metal centers (metal–oxo-metal bonds). The general chemical reaction for the condensation process is given below:

$$\text{M-OH} + \text{XO-M} \rightarrow \text{M-O-M} + \text{XOH} \quad \text{(Condensation)}$$

where M = metal, X = H or alkyl Group (C_nH_{2n+1})

Condensation or polycondensation ultimately results in increasing the viscosity of solvent forming a porous structure maintaining liquid phase called gel. The size and the cross-linking within the colloidal particles mainly depend upon the alkoxide precursor and pH of the solution [13–16].

Step 3 Aging process produces continuous changes in the structure and properties of the gel. During the aging process, polycondensation continues within the localized solution along with reprecipitation of the gel network, which ultimately decreases porosity and increases thickness between colloidal particles

Step 4 The drying process is complicated because water and organic components are detached to form gel which disturbs its structure. There are different drying processes: atmospheric/thermal drying, supercritical drying, and freeze-drying, each one having different implications on the structure of the gel network as shown in Fig. 2. Heating the porous gel at high temperature causes densification [17] and the pores may be removed from gel to get xerogel, which has relatively a low surface area and pore volume and high shrinkage of the gel [18]. On the other hand, in supercritical drying aerogels are formed which have high pore volume and surface area and the original gel network remains almost intact. The third type of drying is done by freezing the solvents to form cryogel; the gel network shrinkage in cryogel is relatively lower than the xerogel. Another important parameter is the relative humidity (RH) during the drying that directly affects the stability and performance of nanomaterials. Particularly, nanofilms dried at lower RH are more stable than those which have been dried at higher RH [19]

Step 5 Lastly, thermal treatment/calcination is performed to drive off the residues and water molecules from the desired sample, the calcination temperature is a very important parameter in controlling the pore size and the density of the material

In the next sections, we present a review on the sol–gel synthesis process for TiO_2, ZnO, SnO_2 and WO_3 NPs and their characterizations.

2.1 Synthesis of TiO_2 nanoparticles using sol–gel method

Sol–gel technique is one of the easiest and efficient methods to synthesize different TiO_2 NPs [20, 21]. Several groups have reported the formation of TiO_2 nanostructures via sol–gel method. Vijayalakshmi et al. [22] have prepared TiO_2 NPs by mixing titanium IV Isopropoxide (TTIP) and ethanol using nitric acid to assist the hydrolysis process. The size of the NPs obtained was around 9 nm and their study showed that TiO_2 NPs with sol–gel method were highly crystalline and had smaller crystallite size as compared to those prepared via hydrothermal method under similar reaction conditions. In another work, Jaroenworaluck et al. [23] prepared TiO_2 NPs by mixing tetraisopropylorthotitanate (TIPT), methanol and ethanol in different molar ratios under stirring. The size of the synthesized anatase NPs was around 10 nm. Furthermore, it was observed that at lower calcination temperature anatase phase was formed and at higher temperatures (600–800 °C) anatase to rutile transformation occurs. In a similar study, Li et al. [20] produced TiO_2 NPs to investigate the phase transformations of TiO_2 NPs.

XRD pattern of multiphase TiO_2 nanostructures is shown in Fig. 3i. The diffraction peaks of different TiO_2 phases are well-matched with their corresponding standard data obtained from their respective JCPDS cards. The presence of sharp diffraction peaks at ~ 25.06°, 48.1°, 54.1°, 55.1° indicate the (101), (200), (105), (211) lattice planes, respectively. Hence, confirming pure and highly crystalline tetragonal anatase TiO_2 phase with the lattice parameters $a = b = 0.377$ nm, and $c = 0.948$ nm (Fig. 3i-a). For brookite TiO_2, the presence of main diffraction peaks at ~ 25.26°, 37.9°, 47.9°, 54.1°, 55.1° indicate the (210), (021), (321), (230), (421) lattice planes, respectively, confirming a pure and crystalline orthorhombic brookite TiO_2 phase with lattice parameters $a = 0.919$ nm, $b = 0.546$ nm and $c = 0.515$ nm (Fig. 3i-b). Similarly, the presence of sharp diffraction peaks at the 27.5°, 36.2°, 39.3°, 41.4°, 44.0° indicate the (110), (101), (200), (111), (210) lattice planes, respectively, confirming a pure and highly crystalline tetragonal rutile

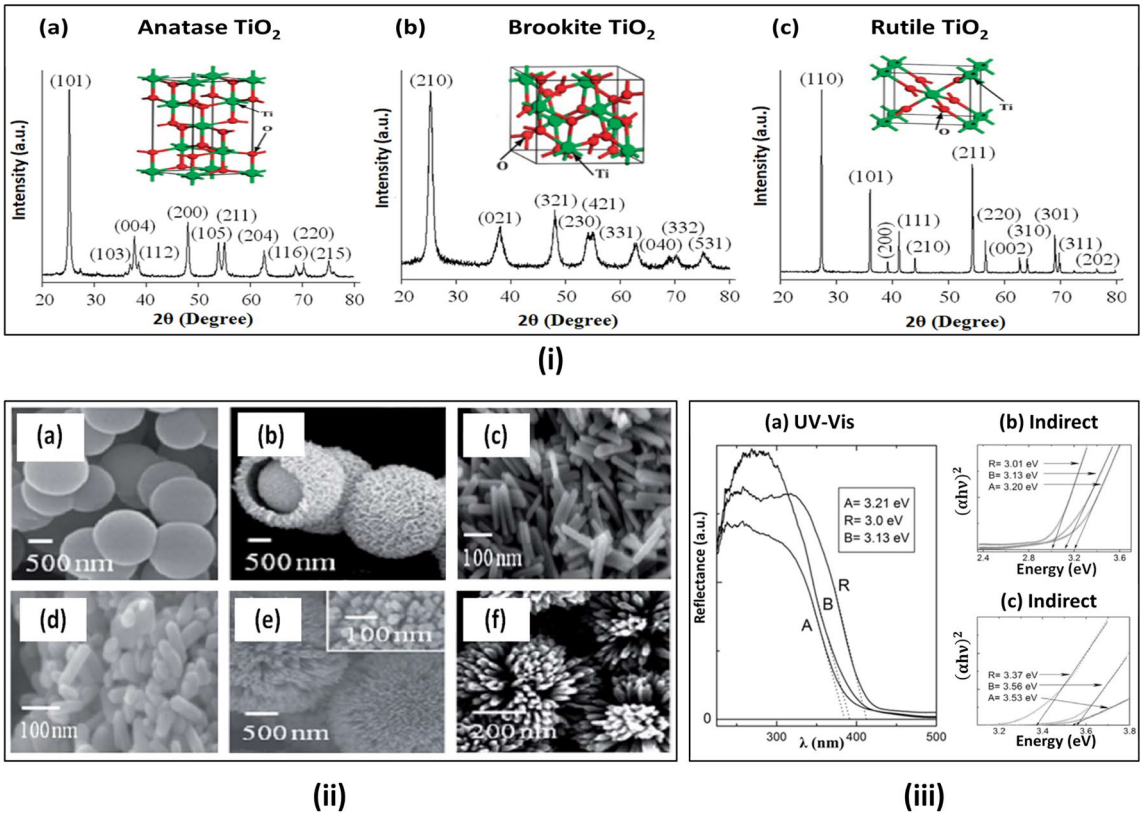

Fig. 3 **i** XRD pattern of multiphase TiO_2: **a** anatase, **b** brookite, **c** rutile TiO_2, **ii** SEM images of TiO_2 nanostructures; **a** and **b** anatase nanostructures, **c** and **d** brookite nanostructures, **e** and **f** rutile nanostructures, **iii** Optical characteristics: **a** UV–Vis reflectance spectra, **b** and **c** optical bandgap evaluation of multiphase TiO_2 NPs from Tauc plots, where the symbols A, B and R correspond to anatase, brookite and rutile-TiO_2 [24–32]

TiO_2 phase with the lattice parameters $a = b = 0.458$ nm, $c = 0.295$ nm (Fig. 3i-c).

Figure 3(ii-a, b) shows the SEM images of the TiO_2 NPs prepared by Li et al. [26] depicting the structural evolution of anatase TiO_2 NPs with the reaction time. After 1-h reaction time, smooth and solid spherical particles were observed and after 1-day reaction time it was observed that small surface platelets formed an urchin like prickly surface developing shell on the NPs. Figure 3(ii-c, d) shows the SEM images of brookite TiO_2 prepared by Kandiel et al. [27] and Zhang et al. [28], depicting brookite rods with diameters up to 25 nm and lengths up to 150 nm. Figure 3(ii-e, f) shows the SEM images of rutile TiO_2 prepared by Sarkar et al. [29] and Bai et al. [30], depicting microspheres of rutile TiO_2 (diameter ~ 2 µm) consisting a cluster of nanorods with diameter ~ 20 nm. From the corresponding high magnified image (inset of Fig. 3ii-e), it can be seen that the nanorods are closely packed with square-shaped ends.

Optical characteristics and related bandgap properties studied by Coronado et al. [31] using UV–Vis spectroscopy are shown in Fig. 3(iii-a–c). The corresponding optical bandgaps of the TiO_2 nanostructures are calculated from the UV–Vis reflectance spectra using the Tauc equation, $(\alpha h\nu)^n = B\left(h\nu - E_g\right)$, where α is the absorption coefficient, $h\nu$ is the energy of the incident photon, B is a constant (characteristic of the material used), E_g is the optical bandgap of the material used and n can have two different values, either 2 for direct or 0.5 for indirect bandgap transitions. The intercept on the x-axis of the Tauc plot $(\alpha h\nu)^n$ versus $h\nu$ gives the optical bandgap energy of the material (Fig. 3iii-b, c) The extrapolation of the reflectance versus wavelength curves determines the optical bandgap energy of TiO_2 NPs giving the values of E_g to be 3.2 eV, 3.13 eV and 3.01 eV (taking $n = 0.5$) and 3.53 eV, 3.56 eV and 3.37 eV (taking $n = 2$) for anatase, brookite and rutile TiO_2, respectively.

XPS spectra of TiO_2 NPs synthesized by Singh et al. [33] showing elemental composition and binding energy of the elements present in the sample (Fig. 4). The curve is fitted using voigt function; curve for O 1s is fitted according to two peaks including Ti–O link at 529.9 eV and O–H link at 532 eV (due to absorbed surface hydroxyl group) [34, 35]. The double peaks of Ti 2p after deconvolution corresponds to Ti $2p_{1/2}$ at 464.4 eV and $Ti_{3/2}$ at 458.7 eV.

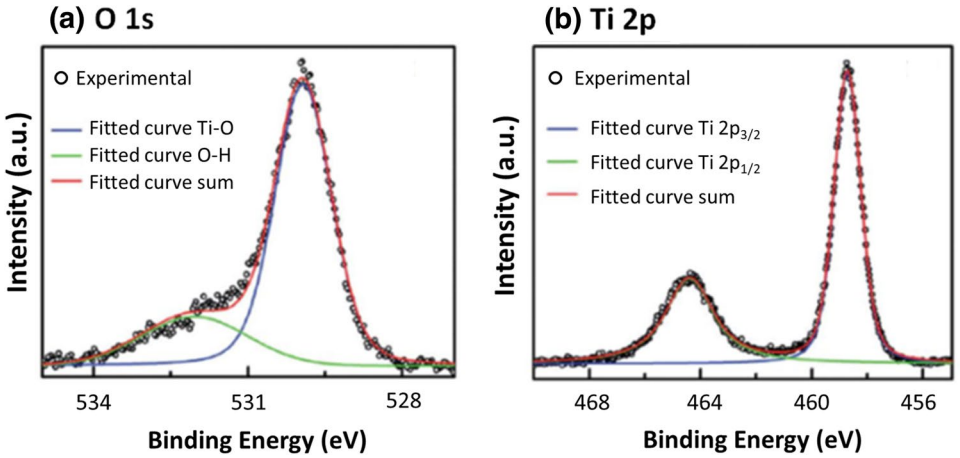

Fig. 4 XPS spectra of **a** O 1*s* and **b** Ti 2*p* of the TiO_2 sample prepared by Singh et al. [33]

Apart from pure TiO_2 NPs, several groups synthesized doped TiO_2 NPs for enhancing their properties for particular application e.g., for degradation of various organic dyes such as rhodamine B, methylene blue (MB), methyl orange (MO) etc. present in waste water for water treatment [36, 37]. Kerkez et al. [38] prepared pure and doped samples of TiO_2 using Titanium(IV) Butoxide, propanol, acetic acid and sulphuric acid as precursors for pure TiO_2 and copper nitrate ($Cu(NO_3)_2{\cdot}3H_2O$), nickel nitrate ($Ni(NO_3)_2{\cdot}6H_2O$), cobalt nitrate ($Co(NO_3)_2{\cdot}6H_2O$), chromium nitrate ($Cr(NO_3)_3{\cdot}9H_2O$), manganese nitrate ($Mn(NO_3)_2{\cdot}5H_2O$) and iron(III) nitrate ($Fe(NO_3)_3{\cdot}9H_2O$) were used as Cu, Ni, Co, Cr, Mn and Fe sources, respectively to prepare the doped samples of TiO_2. They studied the photocatalytic activity of the samples prepared and photocatalytic degradation rates of the MO and MB colorants in presence of visible light and found that the Cu doped TiO_2 sample has highest photocatalytic activity under visible light for both of the dyes. Similarly, Yadav et al. [39] prepared Cu, Fe, Ni, Cr, and Co-doped TiO_2 and undoped TiO_2 nanostructures by sol–gel method and demonstrated photocatalytic dye degradation and antibacterial application.

Peerakiatkhajohn et al. [40] prepared silver doped TiO_2 thin film on polyethylene terephthalate (PET) substrate using Titanium(IV) *n*-butoxide and silver nitrate ($AgNO_3$) as precursors for the preparation of thin films. The Ag/TiO_2 gel obtained from this was directly used for coating on the plastic substrate having potential applications in indoor air pollution treatment and photodegradation of gaseous pollutants such as benzene, toluene, ethylbenzene and xylene. Pan et al. [41] synthesized the surface modified NPs of TiO_2 by octadecyltrimethoxysilane (WD-11) showing potential to be used as nanocomposites in the optical field and as lubricating oil additive. Although NPs already have high surface to volume ratio than their bulk counterparts, but still there is some room for increasing this ratio by having porous NPs. Few studies have showed the simple template-assisted sol–gel process for preparing porous TiO_2 NPs one such study was done by Lakshmi et al. [42]. Their group for the first-time used sol–gel chemistry to prepare semiconductor nanofibrils and tubules within the pores of an alumina template membrane. Wang et al. [43] synthesized porous TiO_2 NPs using tetraethyl orthosilicate (TEOS) as a template forming TiO_2–SiO_2 composite and then selective removal of SiO_2 by dilute hydrofluoric acid (HF) solution. TiO_2 prepared by this method exhibited remarkably improved performance due to its porous structure and large surface area for sensing wide range of RH. A summary of reported synthesis, chemical used, their characteristics and properties is presented in Table 1.

2.2 Synthesis of ZnO nanoparticles using sol–gel method

Solution-based approach (e.g., sol–gel) for synthesis of ZnO NPs is simple and less energy consuming. Due to the simplicity of the sol–gel method, many research groups have synthesized ZnO NPs using it. For instance, Mahato et al. [47] synthesized nanocrystalline ZnO using zinc acetate dehydrate, oxalic acid and ethanol as the precursors by following the method as reported by Hariharan [48] for using it as a decontaminant for the neurotoxic agent called sarin, Ristic et al. [49] prepared nanocrystalline ZnO powder by using Zinc 2-ethylhexanoate containing 1% of ethylene glycol monomethylether, tetramethylammonium($(CH_3)_4NOH$) aqueous solution and isopropanol as precursors. TEM results of the NPs showed that the particles produced by this study had size in the range of 20–50 nm.

Another template-assisted sol–gel method was also used for synthesis of ZnO nanofibres [42]. Yue et al. [50] reported a simple method for synthesis of ZnO nanotubes with porous anodic aluminum oxide (AAO) membranes from two-step anodization in oxalic acid solution. The resulted ZnO nanotubes had size of around 70 nm and thickness of ~ 12 nm.

Table 1 A summary of reported synthesis of TiO_2 nanoparticles via sol–gel method by different research groups

Precursors	Synthesis conditions	Properties	References
TTIP, ethanol, nitric acid	Drying: 2 h, 120 °C Calcination: 2 h, 450 °C	Highly crystalline NPs with size of around 7 nm	[22]
TIPT, methanol, and ethanol	Stirring: 3 h, 55 °C Drying: 5 h, in the vacuum atmosphere Calcination: 3–9 h, 400–800 °C	Anatase at lower calcination temperatures (~ 10 nm) and Rutile at higher calcination temperatures	[23]
$Ti(O\text{-}Bu)_4$, propanol, acetic acid, sulphuric acid, $Cu(NO_3)_2{\cdot}3H_2O$, $Ni(NO_3)_2{\cdot}6H_2O$,$Co(NO_3)_2{\cdot}6H_2O$,$Cr(NO_3)_3{\cdot}9H_2O$, $Mn(NO_3)_2{\cdot}5H_2O$, and Fe $(NO_3)_3{\cdot}9H_2O$	Drying: 15 h, 120 °C Calcination: 2 h, 500 °C For doping: 0.3% M/TiO_2, where M(Cu,Ni,Co,Fe,Mn, and Cr) added to initial solution	Particles with different crystallite sizes were obtained ranging from 37 to 124 nm for doped and undoped samples, Cu/TiO_2 showed highest photocatalytic activity for MB and MO dye	[38]
$Ti(O\text{-}Bu)_4$, ethanol and hydrochloric acid	Drying: 60–80 °C Calcination: 2 h, 200–800 °C	Anatase nano TiO_2 particles with negligible agglomeration and narrow particle size distribution were synthesized	[20]
Titanium (IV) *n*-butoxide, $AgNO_3$, ethanol, nitric acid, acetylacetone	Mixing TiO_2 solution and $AgNO_3$ solution at 80 °C for 8 h	Thin film of TiO_2 and Ag/TiO_2 on PET substrate with film thickness of 85 and 87 nm	[40, 44]
$Ti(O\text{-}Bu)_4$, dehydrated ethanol, glacial acetic acid, WD-11	Stirring: 8 h, at room temperature Drying: 48 h, 80 °C Washing with ethanol and distilled water three times	TiO_2 NPs encapsulated by octadecyltrimethoxysilane were prepared for application in multifunctional lubricating oil additive and fabrication of inorganic/organic nano-composites used in optical fields	[41]
TTIP, isopropanol, deionized water and glacial acetic acid	Stirring: 2 h, pH: 1 Drying: 1 h, 80 °C Calcination: 2 h, 450–700 °C	Slightly agglomerated anatase and rutile phase TiO_2 NPs with size of approximately 13 and 100 nm	[45]
TTIP, hydrochloric acid, ethanol and deionized water	Stirring: 2 h, at room temperature, pH 3–8 Drying: 100 °C, 1 h Calcination: 350–750 °C	Agglomerated particles confirming phase change from anatase to ruitle as calcination temperature increased	[46]
TTIP, ethanol, hydrochloric acid, deionized water	Stirring: 60 s, under ice-bath Immersion of alumina template membrane in sol for: 5–60 s Drying: 400 °C, 6 h	TiO_2 tubules and fibrils prepared in the alumina membrane with 200 nm diameter pores. Tubules were obtained if the membrane was immersed into the sol for a brief period whereas solid TiO_2 fibrils were obtained after long immersion times	[42]
$Ti(O\text{-}Bu)_4$, TEOS, acetic acid, ethanol, nitric acid and deionized water	Stirring: 5 h Add TEOS in sol and then drying: 70 °C, 2 h Calcination: 450 °C, 2 h Washing with HF solution 4%	Porous TiO_2 with BET as high as 118 $m^2\ g^{-1}$ for humidity sensing	[43]

Mayekar et al. [51] studied the role of temperature and sodium hydroxide in the preparation of zinc oxide NPs, their study showed that the particle size increases with increase in the temperature and also with the increase in the sodium hydroxide concentration.

Figure 5i is showing the FESEM and SEM images for the 0 Dimensional, 1 Dimensional, 2 Dimensional and 3 Dimensional ZnO structures of different shapes and sizes. Figure 5(i-a) shows the spherical ZnO NPs having a size of around 80 nm prepared by Zavar [52] after calcination for 2 h at 350 °C. SEM image of 1D ZnO nanostructures having length and diameter in the range of about 3 µm and 200–500 nm, respectively are shown in Fig. 5(i-b) [53]. SEM micrograph of ZnO nanosheets (Fig. 5(i-c)) prepared by Ju et al. [54] shows the network of uniform and homogenous nanosheets with a large size and density. Highly uniform flower-like particles consisted of hexagonal nanorods prepared by Yue et al. [55] have been shown in Fig. 5(i-d). The typical size of these individual nanorods ranged from 300 to 800 nm in diameter and about 2–3 µm in length.

XRD pattern of the synthesized NPs prepared as reported in a particular study [56] has been shown in Fig. 5ii. The observed experimental peaks are fitted to the standard JCPDS card values corresponding to the ZnO reflections from (100), (002), (101), (102), (110) and (103) planes, confirming the ZnO hexagonal wurtzite structure. The typical UV–Vis absorption spectrum of ZnO NPs has been shown in Fig. 5(iii-a) where it can be seen that the NPs exhibit strong absorption in UV region (around 279 nm). The determination of energy bandgap (3.76 eV) is done by plotting Tauc curve shown in Fig. 5(iii-b). This value of bandgap is slightly higher than the actual value of bandgap for ZnO. This enhancement in bandgap occurs due to the quantum confinement of carrier within the nano dimensions [57].

Figure 6a shows the XPS spectra of ZnO NPs prepared via sol–gel method by Zhang et al. [58]. The survey scan is showing the presence of zinc, oxygen and carbon (impurity). Figure 6b, c is showing the high-resolution XPS spectra of Zn 2*p* and O 1*s*, respectively of ZnO nanorods samples prepared by Navaneethan et al. [59]. The Zn $2p_{1/2}$ and Zn $2p_{3/2}$ peaks were observed at 1046.8 eV and 1023.8 eV, indicating the presence of bivalent oxidation state in the sample [60]. The O 1*s* peak positioned at the binding energy of 530.8 eV was assigned to O^{2-} ions in the Zn–O bonding of the hexagonal wurtzite structure of ZnO and the peak located at 523.3 eV was associated with O^{-} and O^{2-} ions in oxygen deficient regions in the sample matrix [61].

Further, ZnO nanostructures doped by Al, Ga, Sn, Ni, In, N and Li have been widely studied by some research groups

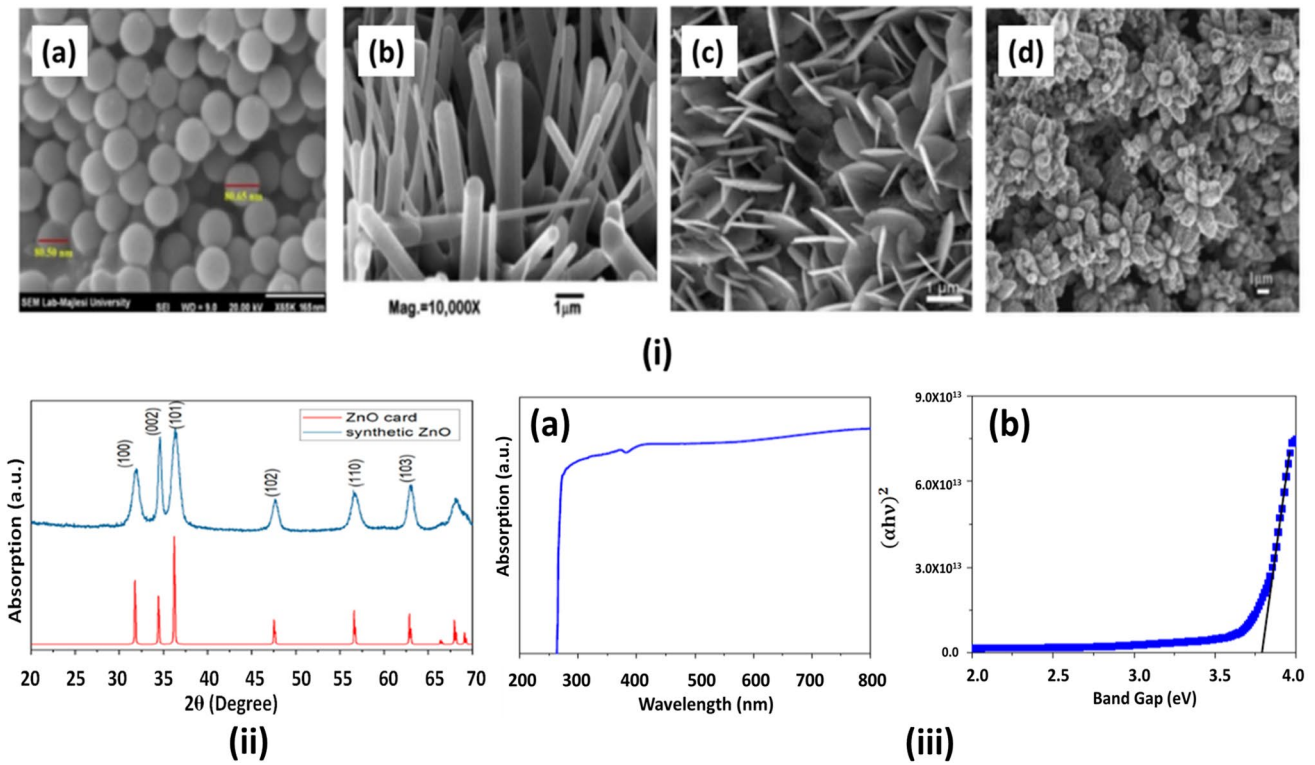

Fig. 5 **i** FESEM and SEM images for **a** 0D, **b** 1D, **c** 2D, **d** 3D zinc oxides [52–55], **ii** XRD pattern of Synthetic ZnO NPs and the standard ZnO wurtzite structure from JCPDS card No. 36-1451 [56] and **iii-a** UV–Vis spectrum of ZnO NPs and **b** Tauc plot for determination of bandgap of ZnO NPs [57]

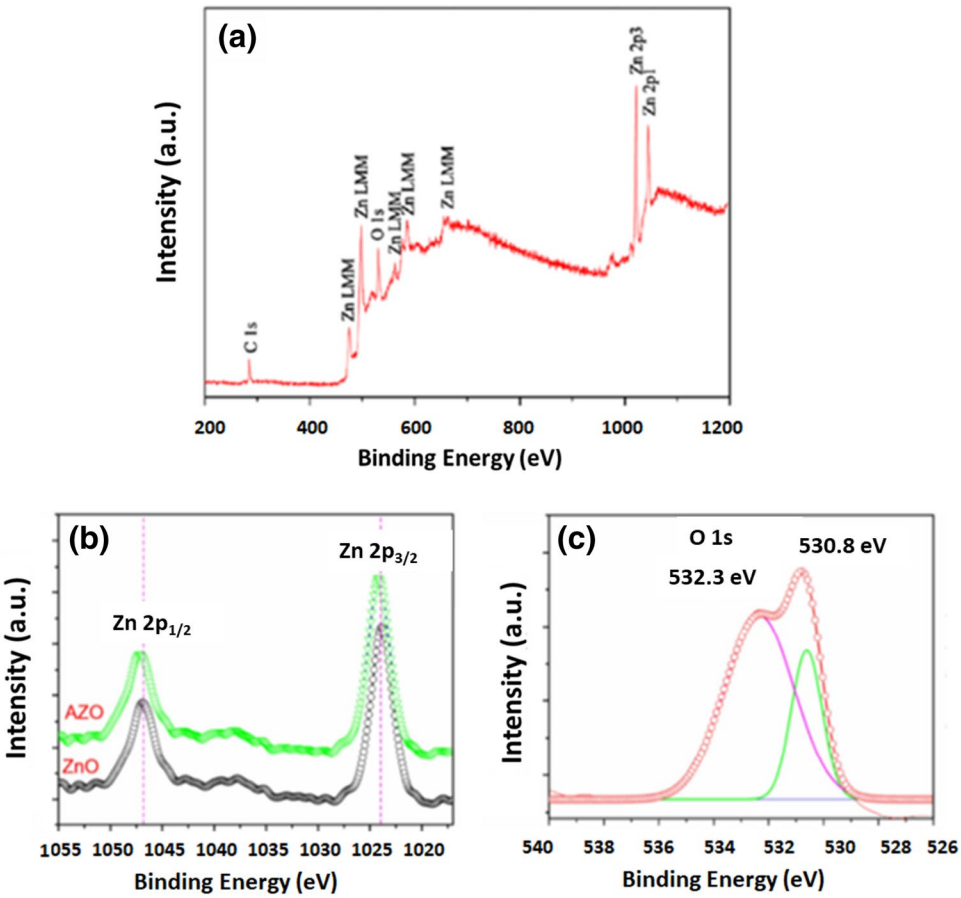

Fig. 6 **a** XPS spectra of ZnO NPs annealed in air at 800 °C prepared by sol–gel method [58] **b** high-resolution XPS spectra of Zn $2p_{1/2}$ and Zn $2p_{3/2}$ and **c** high-resolution XPS spectra of O 1*s* [59]

for their structural, optoelectronics, luminescence, photocatalytic, impedance and thermal properties [62–71]. Similarly, doped ZnO nanostructures have been reported by Ullah et al. and Hossain et al. [72, 73] to study the photocatalytic degradation of organic dyes with the use of manganese-doped zinc oxide NPs which were prepared by sol–gel technique. ZnO doped and undoped colloids were made using zinc acetate, sodium hydroxide, ethanol and manganese acetate (dopant).

Also, ZnO thin films have been reported by some research groups. Natsume et al. [74] prepared ZnO thin films on Pyrex glass substrate by spin coating various layers of the solution of zinc acetate dihydrate and methanol followed by annealing in the temperature range of 500–575 °C to study the resistivity of the films. They found out a minimum film resistivity of 28.2 Ω cm was at an annealing temperature of 525 °C. Nagase et al. [75] reported a method to prepare ZnO films by spin coating on quartz substrate by using KrF excimer laser irradiation of sol–gel derived precursors prepared by zinc acetate and monoethanolamine dissolved in 2-methoxymethanol. Laser irradiation resulted in two types of effects on crystalline ZnO film (i) Irradiation at low energy fluence produces low crystallinity with weak orientation and (ii) irradiation at high energy fluence produces high crystallinity with strong orientation. A summary of reported synthesis, chemical used, their characteristics and properties is presented in Table 2.

2.3 Synthesis of SnO_2 nanoparticles using sol–gel method

Different research groups performed synthesis of SnO_2 NPs using sol–gel method. Gu et al. [76] prepared nanoscale SnO_2 by simple sol–gel method using tin chloride pentahydrate ($SnCl_4{\cdot}5H_2O$) and ammonia solution (NH_4OH). The reported diameter of the prepared NPs was about 2.6 nm. Adnan et al. [77] also prepared the SnO_2 NPs using tin chloride pentahydrate ($SnCl_4.5H_2O$) and ammonia solution (NH_4OH 25%). The high amount of ammonia leads to decrease in surface area and agglomeration of particles. Their study showed that SnO_2 prepared at high alkaline condition (pH 10.2) exhibited higher catalytic activity in the hydrogenation reaction of styrene. Zhang et al. [78] used Nitric acid, granulated tin and aqueous ammonia (25%) as precursors and used citric acid as complexing agent. They showed that the use of citric acid slows down the hydrolysis and condensation of the precursor and thus inducing nucleation at early stage of the process resulting in monodispersed particles ranging from 2.8 to 5.1 nm in size. De Monredon

Table 2 A summary of reported synthesis of ZnO nanoparticles via sol–gel method by different research groups

Precursors	Synthesis conditions	Properties	References
Zinc acetate dehydrate, oxalic acid and ethanol	Stirring: 60 °C Drying: 24 h, 80 °C Calcination: 500 °C	Randomly oriented aggregates of NPs and nanorods with variable sizes. With average crystallite size of ~ 55 nm for decontamination of sarin were produced	[47, 48]
Zinc 2-ethylhexanoate, $((CH_3)_4NOH)$ and isopropanol	Stirring: at room temperature Aging: 30 min–24 h Drying: 60 °C	Particles with size range of 20–50 nm	[49]
Zinc acetate, diethanolamine, ethanol	Stirring: at room temperature The ultrathin Anodic Aluminum Oxide (AAO) membrane then immersed into the sol for 30 min Annealing: 2 h, 500 °C	ZnO nanotubes with a diameter of 70 nm with thickness of 12 nm were produced in AAO membrane	[50]
Zinc acetate, sodium hydroxide, ethanol and manganese acetate (used as dopant)	Heating in water bath at 60–65 °C, for 2 h Centrifuge: at 4000 rpm, 20 min	Polycrystalline structure of different sizes ranging from 21 m to 73 nm were produced, ZnO:Mn^{2+} having higher photocatalytic activity than virgin ZnO under visible light irradiation	[72, 73]
Zinc chloride, sodium hydroxide	Stirring: 80 °C Drying: 2 h, 80–100 °C NaOH concentration: 2–10 M	Particles with 20–350 nm size were produced having shape varying from spherical to rod-like structures	[51]
Zinc acetate dihydrate and methanol	Spin coating: 20 s, 3000 rpm Drying: 10 min, 80 °C Annealing: 20 min, 500–575 °C	Nanofilm with thickness of 160–230 nm on Pyrex glass substrate	[74]
Zinc acetate, monoethanolamine, 2-methoxymethanol	Spin coating: 2000 rpm Drying: 10 min, 473 or 573 K Irradiation of dried film by KrF excimer LASER ($(\lambda = 248$ nm, 22 ns Full Width Half Maximum)	ZnO nanofilms with thickness of 35–60 nm were obtained	[75]

et al. [79] prepared monodispersed crystalline NPs of SnO_2 by hydrolysis of tin isopropoxide with acetylacetone and p-toluene sulfonic acid. Ristic et al. [80] studied the size dependence of nanocrystalline SnO_2 on the synthesis route. They used Sn(IV) chloride ($SnCl_4$), Sn(IV)-isopropoxide ($Sn(OCH(CH_3)_2)_4$) and isopropanol as precursors. The average particle size reported in their study was around 2.05 nm found by the low-frequency Raman Scattering method. Aziz et al. [81] synthesized tetragonal phase SnO_2 NPs using tin chloride ($SnCl_2{\cdot}2H_2O$) and polyethylene glycol (PEG), ethanol and acetylacetone. Results showed that the SnO_2 calcined at lower temperature with the incorporation of high molecular weight of PEG results in non-uniform tiny crystallites compared to the others. Gnanam et al. [82] prepared tin oxide NPs using different solvents such as methanol, ethanol, and water to study their effect on the optical properties of SnO_2 using tin tetrachloride pentahydrate ($SnCl_4{\cdot}5H_2O$) as a precursor to form sols. The SnO_2 nanocrystallites prepared in methanol, ethanol, and water formed with a particle size of 3.9, 4.5 and 5 nm, respectively.

From the reported work by Gnanam et al. [82], TEM and HR-TEM images of the SnO_2 NPs to study the morphologies and particle size have been shown in Fig. 7i. Figure 7(i-a) shows methanol mediated SnO_2 NPs with spherical morphology of size about 3 nm. Figure 7(i-b, c) shows TEM pattern of sample prepared in ethanol and water and the size of the NPs was 4.5 nm and 5 nm, respectively. Figure 7(i-d–f) shows the high-resolution TEM (HR-TEM) image of the SnO_2 NPs calcined at 400 °C, for 2 h. It shows clear lattice fringes, indicating the established crystallinity of SnO_2 powders. The XRD pattern of the SnO_2 NPs prepared with different solvents namely methanol, ethanol and water calcined at 400 °C for 2 h have been shown in Fig. 7ii, which corresponds to the tetragonal rutile structure of SnO_2 having lattice parameters $a = b = 0.4739$ nm and $c = 0.316$ nm. The XRD pattern of the organic mediated sample (Fig. 7ii-a, b) shows slight broadening of peaks compared to that of the aqueous mediated sample (Fig. 7ii-c). The room temperature UV–Visible spectrum is shown in Fig. 7(iii). The methanol mediated SnO_2 NPs has the absorption edge at 312 nm (Fig. 7iii-a), which is smaller than the band edges observed at 323 and 337 nm for ethanol and water as shown in Fig. 7(iii-b, c) and the corresponding bandgap energies calculated to be 3.97, 3.83 and 3.68 eV for methanol, ethanol and water-mediated SnO_2 NPs, respectively which is larger than the bulk SnO_2.

The XPS spectra of SnO_2 NPs prepared by Al-Hada et al. [83] are shown in Fig. 8a. The presence of Sn and

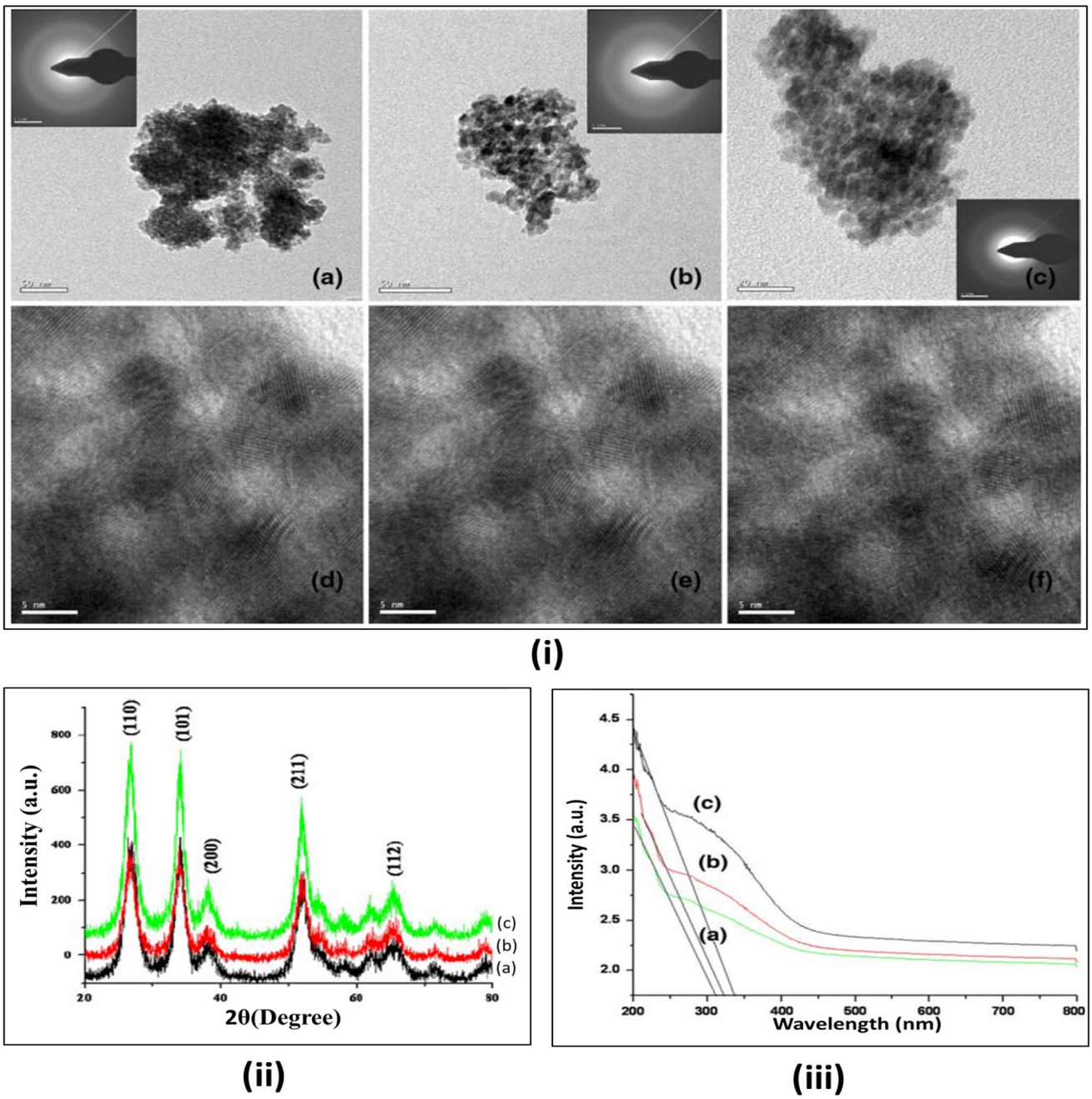

Fig. 7 **i** TEM of the as-prepared SnO_2 NPs mediated in **a** methanol, **b** ethanol, and **c** water. HR-TEM images of the as-prepared SnO_2 NPs mediated in **d** methanol, **e** ethanol, and **f** water, **ii** XRD pattern of SnO_2 NPs mediated in methanol (**a**), ethanol (**b**), and water (**c**), **iii** UV–Vis absorption spectra of SnO_2 NPs mediated in methanol (**a**), ethanol (**b**), and water (**c**) [82]

O elements is confirmed by the XPS curve. The deconvoluted Sn peaks i.e., Sn $3d_{3/2}$ and Sn $3d_{5/2}$ are shown in Fig. 8b with binding energies of 494.9 eV and 487.8 eV, respectively which are also in good agreement with the research led by other groups [84–86]. The deconvoluted O 1*s* spectra (Fig. 8c) demonstrate binding energies at 529.7 eV and 531.1 eV which is correlated with SnO_2 [87, 88]. A summary of reported synthesis, the chemical used, their characteristics and properties are presented in Table 3.

2.4 Synthesis of WO_3 nanoparticles using sol–gel method

Different structures of WO_3 like NPs, nanofilms and nanocomposites have been prepared via sol–gel method by

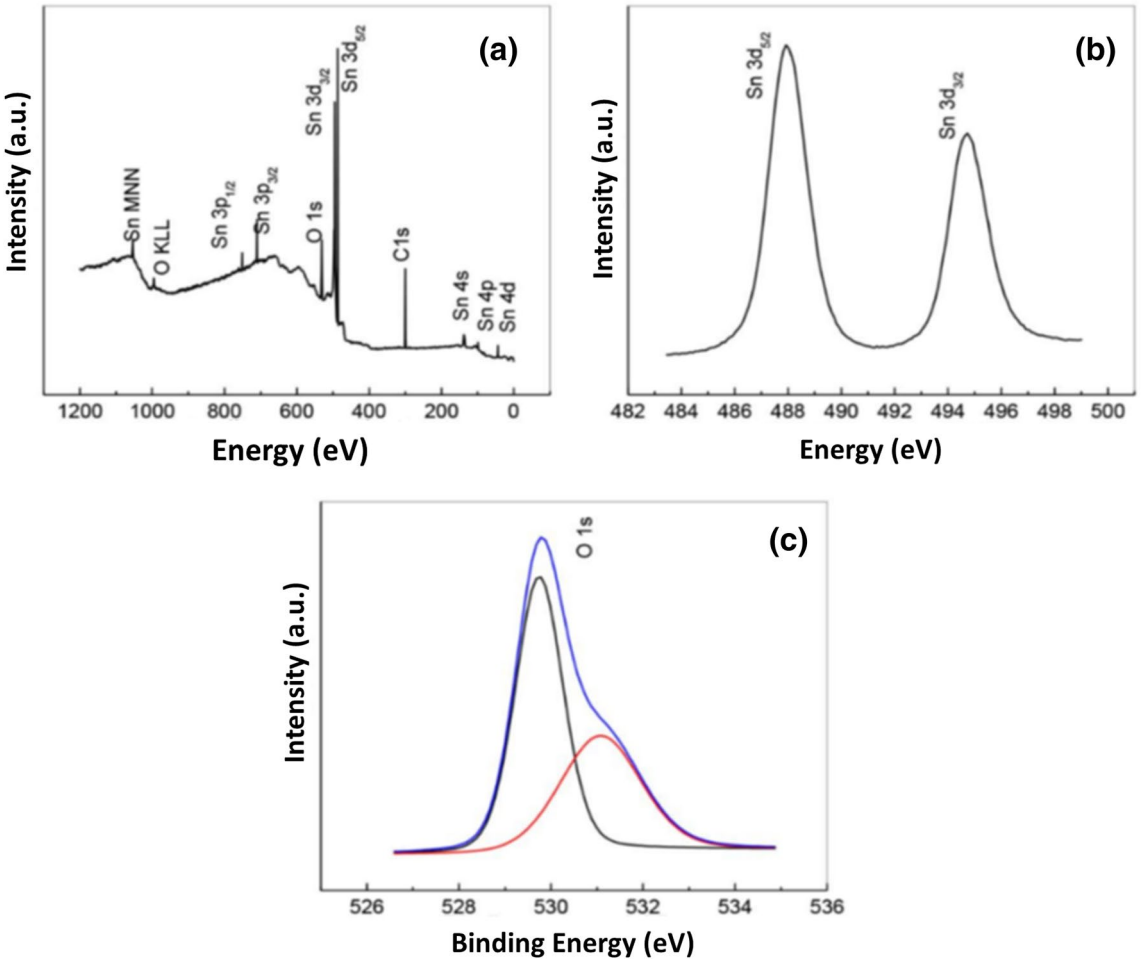

Fig. 8 **a** XPS spectra of SnO_2 NPs, **b** Sn $3d_{5/2}$ and Sn $3d_{3/2}$ XPS spectra, **c** O 1*s* XPS spectra [83]

various groups [89–91]. Shi et al. [92] prepared WO_3 NPs in the range of 25–100 nm for detection of acetone rendering its potential application in the diagnosis of diabetes. For the synthesis of NPs, a solution of peroxopolytungstic acid (PTA) was prepared from tungsten powder, hydrogen peroxide and a block copolymer $EO_{20}PO_{70}EO_{20}$. The developed sensors possess a detection limit down to ~ 0.05 ppm.

Susanti et al. [93] prepared nano-WO_3 based gas sensor via sol–gel method to detect carbon monoxide (CO) gas using a mixture of tungsten hexachloride and ethanol to prepare the tungsten alkoxide precursor $W(OC_2H_5)_6$ and a surfactant (Triton X-100) to prepare the WO_3 gels. Their result showed that the sensitivity of the material toward CO gas was dependent on the calcination temperature. Santato et al. [94] prepared mesoporous semiconducting WO_3 films using colloidal solution from tungstic acid, sodium tungstate, stabilized by an organic additive such as polyethyleneglycol (PEG) 300. Their study showed that thin (less than 1 µm thick) nanocrystalline WO_3 films have several interesting features such as excellent adherence and mechanical stability, open mesoporous structure and good transparency, making them suitable candidates for electrochromic device applications.

Figure 9i shows the XRD patterns of the different forms of WO_3 matched with their corresponding JCPDS card: (a) hexagonal WO_3 (b) monoclinic WO_3 and (c) orthorhombic WO_3 [95, 96]. UV–Vis spectrum of the WO_3 nanocubes showing the absorption at about 473 nm and bandgap determined by Tauc plot with value of 2.58 eV is shown in Fig. 10ii [97]. TEM and SEM image of WO_3 NPs prepared by Shi. et al. [92] having spherical shape with size ranging from 25 to 100 nm is shown in Fig. 10iii.

XPS spectra of nanostructured WO_3 thin films prepared by Breedon et al. [90] have been discussed in Fig. 10a which reveal the presence of tungsten, oxygen, sodium and carbon. The Spectra of O 1*s* and W 4f7 is shown in Fig. 10b and c, respectively. The Na 1*s* peak at 1072 eV was found due to the presence of the by-products of the sodium tungstate precursor. The O 1*s* spectra of the prepared sample shown in Fig. 10b, showing a weak oxygen

Table 3 A summary of reported synthesis of SnO_2 nanoparticles via sol–gel method by different research groups

Precursors	Synthesis conditions	Properties	References
$SnCl_4{\cdot}5H_2O$, NH_4OH solution	Drying: several hours, 80 °C Calcination: 2 h, 400-600 °C	NPs of diameter of about 2.6 nm were formed	[76]
$SnCl_4{\cdot}5H_2O$, NH_4OH solution (25%)	Stirring: 2 h, 30-90 °C pH values: 1 to 10.2 Washing with ethanol till pH is 7 Drying: 24 h, 80 °C in air Calcination: 2 h, 400 °C	Particles size of 4 to 5.6 nm and the surface area was found to be in between 76 to 114 $m^2\ g^{-1}$ depending on the reaction parameters. Catalytic activities of prepared SnO_2 NPs were investigated in hydrogenation of styrene	[77]
Nitric acid, granulated tin, aqueous ammonia (25%)and citric acid (complexing agent)	Stirring: 2 h, 100 °C Drying: 5 h, 100 °C in air Calcination: 2 h, 300–500 °C	monodispersed particles ranging from 2.8 to 5.1 nm in size and 289–143$m^2\ g^{-1}$	[78]
$Sn(OCH(CH_3)_2)_4$, acetylacetone p-toluenesulfonic acid	Stirring: 2 h, room temperature Aging: 24–48 h, 60 °C Heat treatment: 2 h, 150–1000 °C	Monodisperse spheroidal crystalline NPs of tin oxide, the mean size of the cassiterite oxide core is around 1–2 nm	[72]
$SnCl_4$, $Sn(OCH(CH_3)_2)_4$ and isopropanol	Stirring: 3 h, 100 °C Drying: 48 h, 55 °C Calcination: 4 h, 600 °C	Particles with average size of 2.05 nm were formed	[80]
Tin chloride, polyethylene glycol (PEG), ethanol and acetylacetone	Stirring: 5 h, 80 °C Aging: 72 h, 30 °C Drying: 30 min, 100 °C Calcination: 1 h, 450–600 °C	NPs with size in the range of 16–32 nm	[81]
Tin tetrachloride pentahydrate, methanol, ethanol and water	Drying: 5 h, 80 °C Calcination: 2 h, 400 °C	The particle sizes of the SnO_2 prepared in methanol, ethanol, and water were 3.9, 4.5 and 5 nm, respectively	[82]

peak at 533.2 eV which is due to the oxygen atoms bound with or in WO_3 and the main peak found at 530.6 eV. As the annealing temperature increased the smaller peak diminishes due to the expulsion of the water molecules and the main oxygen peak intensifies. The W 4*f* orbital is resolved in Fig. 10c into W $4f_{5/2}$ and W$4f_{7/2}$ at 37.5 eV and 35.4 eV, no evidence of the formation of substoichiometric WO_{3-x} was found as no peak mainly occurring at 34.8 eV as seen by other groups [98] can be seen here.

Nanocomposites prepared by Yao et al. [99] showed the formation of colloids to improve photochromism of WO_3 by the combination of TiO_2, most electrons will accumulate in WO_3 resulting in the efficient suppression of the recombination process of electrons and holes after the combination. They used Sodium tungstate ($Na_2WO_4{\cdot}2H_2O$), oxalic acid ($H_2C_2O_4{\cdot}2H_2O$) and titanium butoxide $Ti(O\text{-}Bu)_4$ to form TiO_2 and WO_3 colloidal sols. Benoit et al. [100] reported a simple approach to decorate ordered TiO_2 nanotube layers with WO_3 to form WO_3–TiO_2 nanocomposite by using WCl_6, ethanol and annealed TiO_2 nanotubes as precursors. Their results showed that TiO_2 decorated with WO_3 led to remarkable enhancement in electrochromic properties. A summary of reported synthesis, chemical used, their characteristics and properties is presented in Table 4.

3 Applications of metal oxide nanoparticles

MONPs can be useful in different areas ranging from cosmetics, color pigments, screen coatings, photovoltaics, photocatalysis, drug delivery, etc. (Fig. 11). Different applications of MONPs are discussed below:

3.1 Photocatalysis applications

MONPs can produce photogenerated charge carriers upon excitation with required amount of light energy and having technological significance in environmental remediation and electronics. The abundant MONPs (TiO_2, ZnO, SnO_2 and WO_3) have been used as photocatalyst due to their controllable optical and electronic properties. Most of the MONPs are investigated for use as antibacterial, self-cleaning, and deodorization system [102, 103].

For example, the wastewater can be purified by the removal of harmful bacteria and other organic pollutants with semiconducting photocatalysis process [104]. The mechanism of photocatalysis involving MONPs for photodegradation of organic dyes is described in Fig. 12 and the reactions taking place under this process can be explained by Eqs. (1)–(7) [105]

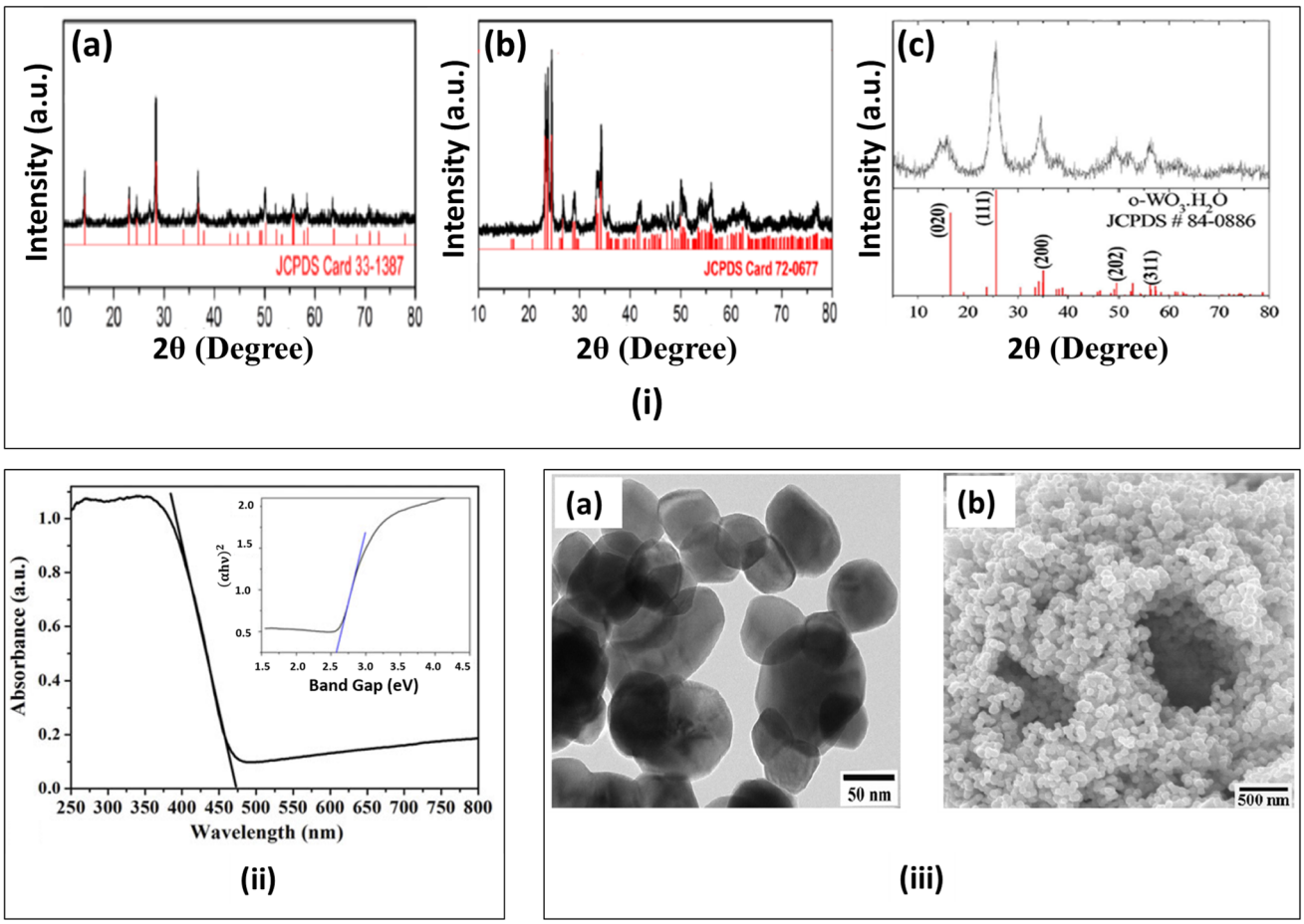

Fig. 9 **i** XRD patterns of WO_3: hexagonal tungsten trioxide (**a**), monoclinic WO_3 (**b**), orthorhombic WO_3 (**c**), **ii** UV–Vis spectra and inset is plot of $(\alpha h\nu)^n$ versus $h\nu$ photon energy (Tauc plot), **iii** Bright-field TEM image of WO_3 nanocrystals (**a**), SEM micrograph of the WO_3 nanocrystals [92, 95–97]

$$\text{MONPs} + h\nu \rightarrow \text{Me}^{-}_{\text{CB}} + \text{Mh}^{+}_{\text{VB}} \quad (1)$$

$$\text{Mh}^{+}_{\text{VB}} + \text{H}_2\text{O} \rightarrow \text{H}^{+} + \text{OH}^{\cdot} \quad (2)$$

$$\text{Mh}^{+}_{\text{VB}} + \text{OH}^{-} \rightarrow \text{OH}^{\cdot} \quad (3)$$

$$\text{Me}^{-}_{\text{CB}} + \text{O}_2 \rightarrow \text{O}_2^{\cdot -} \quad (4)$$

$$\text{Organic pollutant} + \text{OH}^{\cdot} \rightarrow \text{degradation products} \quad (5)$$

$$\text{Organic pollutant} + \text{Mh}^{+}_{\text{VB}} \rightarrow \text{oxidation products} \quad (6)$$

$$\text{Organic pollutant} + \text{Me}^{-}_{\text{CB}} \rightarrow \text{reduction products} \quad (7)$$

where $h\nu$ = energy of photon, $\text{Me}^{-}_{\text{CB}}$ = conduction band electron in MONPs, $\text{Mh}^{+}_{\text{VB}}$ = valence band hole in MONPs.

The photocatalytic antibacterial applications of TiO_2 based nanostructures were summarized by Yadav et al. [106]. Similarly ZnO, SnO_2 and WO_3 NPs have also shown antibacterial and high photocatalytic activities as reported in different works [107–109].

3.2 Photovoltaics applications

Since several decades, photovoltaic technologies utilize semiconducting metal oxides. The outstanding flexibility of their optoelectronic properties and simple preparation method offers metal oxides an exclusive place to next-generation photovoltaics. Moreover, their outstanding capability to preserve or improve the device characteristics allows their application in semi-transparent and flexible solar cell devices, and printable electronics [110–112].

MONPs are used for different purposes in solar cells e.g., as an electron transport layer/hole blocking layer and mesoporous scaffolds in perovskite solar cells (PSCs) and dye sensitized solar cells (DSSCs) (Fig. 13b, c).

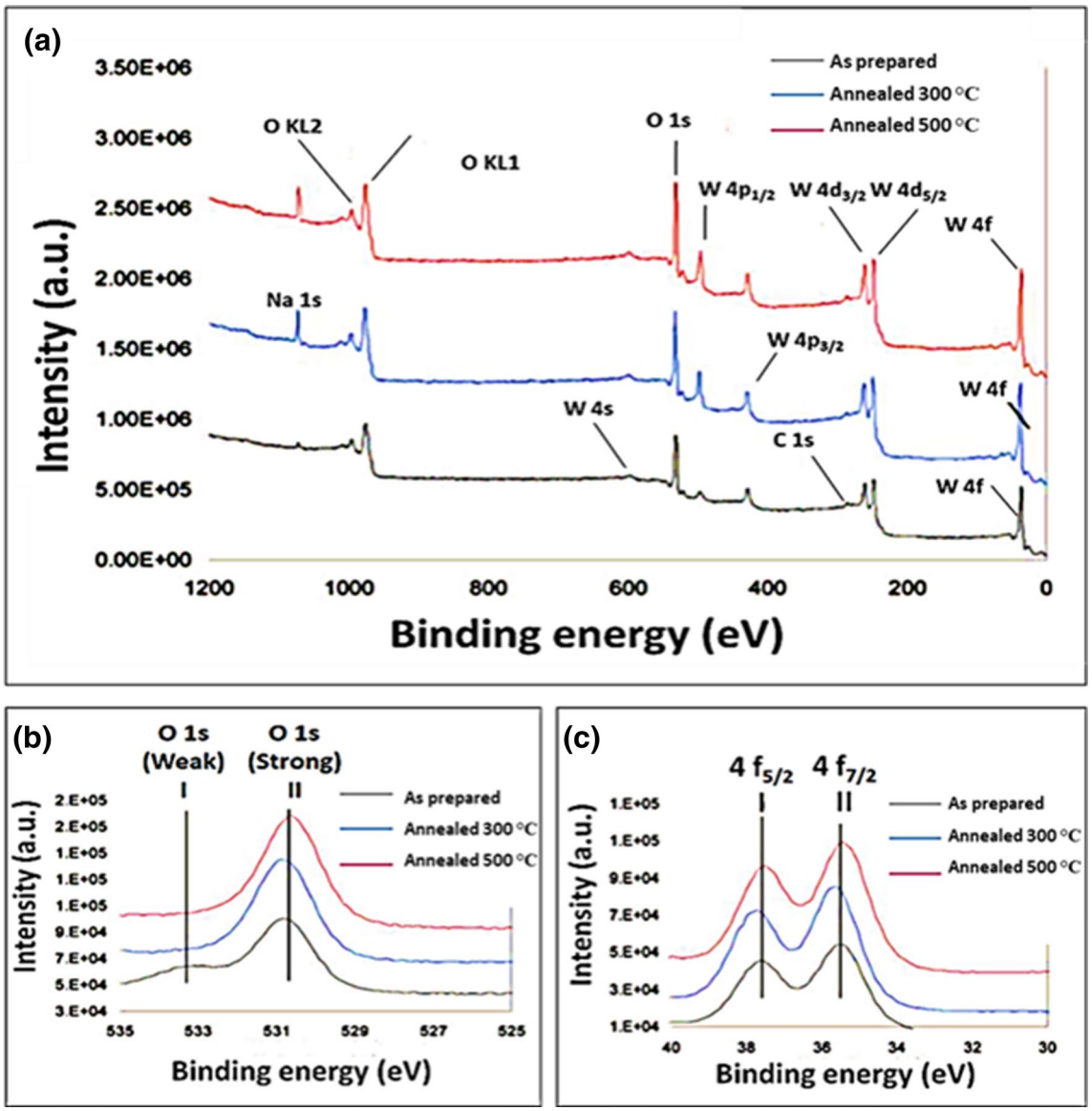

Fig. 10 **a** XPS survey spectra of tungsten oxide samples, XPS of tungsten oxide hydrate and annealed samples **b** O 1*s* and **c** W 4f7 [90]

Significant light scattering effect has been shown by MONPs when embedded in the organic materials [112, 117–120]. In PSCs, it is seen that the LUMO level of the perovskite light absorber layer is little higher than the conduction band edge of the MONPs (Fig. 13a), thus it is possible for perovskite material to transfer its electron to the MONPs layer for facilitating efficient charge transfer and collection.

TiO_2 NPs are one of the most used materials for photovoltaic applications; it's been mainly used in PSC and DSSC devices [121, 122]. For devices on flexible substrate, ZnO is preferred candidate owing to its higher electron mobility in comparison to TiO_2 and low-temperature synthesis which requires no heating/sintering [123]. Mesoporous SnO_2 thin films can also be used to replace mesoporous TiO_2 scaffold layers in PSCs to achieve good power conversion efficiencies [124]. WO_3 nanosheets coated with thin layer of TiO_2 also resulted in good electron transport layer in PSC [125].

3.3 Gas sensing applications

MONPs gas sensors are the most investigated group of gas sensors owing to their large surface to volume ratio and high surface reactivity. One of the challenges for MONPs gas sensors is to achieve high selectivity [126]. Several MONPs have been used for sensing combustible, reducing, or oxidizing gases by observing electrical conductivity [127].

Table 4 A summary of reported synthesis of WO_3 nanoparticles via sol–gel method by different research groups

Precursors	Synthesis conditions	Properties	References
Tungsten hexachloride, ethanol, ammonia, $AgNO_3$, ammonia hydroxide, and Triton X-100	Stirring: 24 h in ice-bath Spin coating of gel: (i) 30 s, 500 rpm (ii) 90 s, 2000 rpm Calcination: 1 h, 300–600 °C	WO_3 coated on Alumina wafers having crystallite size from 6.4-39.3 nm to be used for CO gas detection	[93]
Tungsten (VI) oxytetrachloride, isopropanol	Stirring: one night, room temperature Dip coating: pull rate of 5.6 mm/s Drying: overnight, 80 °C	WO_3 film deposited on flexible PET/ITO substrate showing good electrochromic properties	[89]
Tungsten powder, hydrogen peroxide, block copolymer $EO_{20}PO_{70}EO_{20}$ and ethanol	Stirring: 2 h, 80 °C Calcination: 5 h, 500 °C	Spherical NPs having a size in the range of 25–100 nm to be used as sensors for detecting acetone	[101]
Nitric acid and sodium tungstate	Spin coating: 8000 rpm Flow rate: 0.25–5.0 mL/min Drying: 24–72 h in (a) 35% and (b) 55% RH	Rectangular or square nanoplatelets having thickness of the order of 10-30 nm used for fabrication of NO_2 gas sensors	[90]
Tungstic acid, sodium tungstate and PEG 300	Drying: 10 min, room temperature Annealing: 30 min, 400–550 °C	Thin (less than 1um thick) nanocrystalline WO_3 films prepared for electrochromic device applications	[94]
Titanium butoxide, ethanol, acetic acid, and ammonium tungstate	Stirring: 2 h Drying of the gel at the desired temperature Sintering: 2 h, 973 K	WO_x/TiO_2 nanocomposite with particles size of ~ 22.5–23.4 nm was formed and showed greater photoactivity than pure TiO_2	[91]
Sodium tungstate, oxalic acid, titanium butoxide	Purging of Argon in WO_3 suspension: 15 min pH < 1 Sonication of WO_3 and TiO_2 colloids	WO_3/TiO_2 composite material having more photochromism than pure WO_3 colloids	[99]
Tungsten hexachloride, ethanol, and annealed TiO_2 nanotubes	Temperature: 1 h, 70 °C Sample rinsed in ethanol and dried in a nitrogen stream Annealing: 1 h, 450 °C	TiO_2 decorated with WO_3 inducing remarkable enhancement in electrochromic properties	[100]
Tungsten hexachloride, ethanol, 2,4-Pentanedione and deionized water	Argon Purging in sol Immersion of alumina membrane: 1 min Drying of membrane: 550 °C, 6 h	WO_3 fibrils obtained within the pores of the 200 nm diameter alumina template membrane, the fibrils were 200 nm in diameter and 50 μm in length	[42]

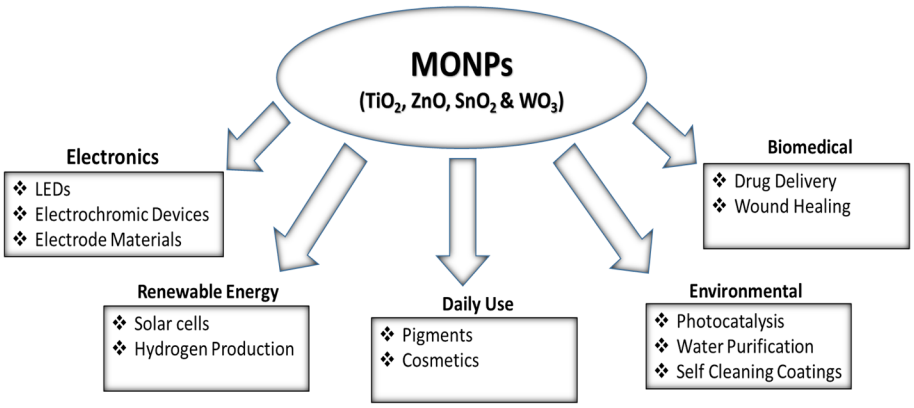

Fig. 11 Different applications of TiO_2, ZnO, SnO_2 and WO_3 NPs

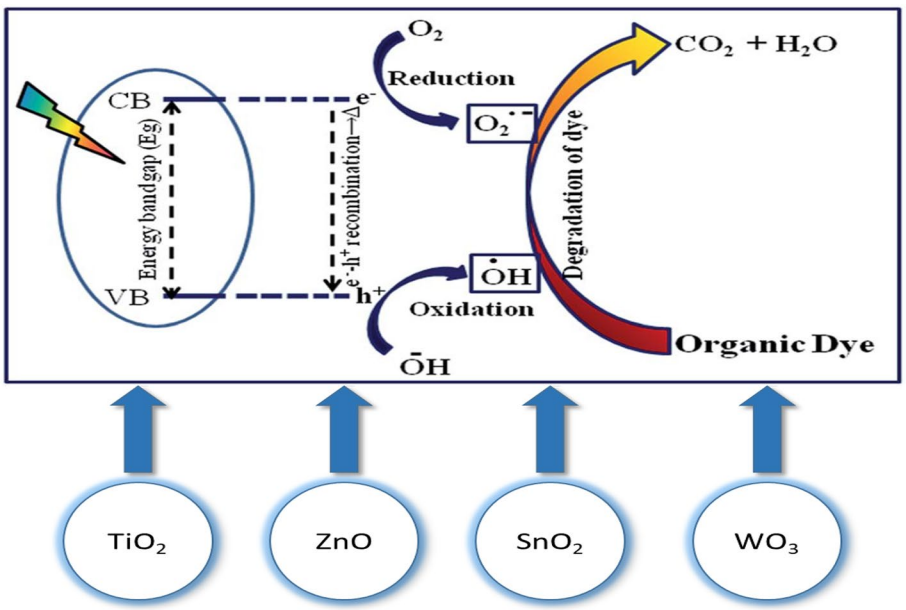

Fig. 12 Mechanism of photodegradation of organic dyes under illumination for different MONPs [102]

A schematic representation of gas sensing device is shown in Fig. 14. The interaction with the surrounding atmosphere changes the conductivity of metal oxide and because of its transducer function electrical signal is transmitted to the electrode. The indirect heating of the device is used to change its electrical conductivity. A promising research has been done for metal oxide-based gas sensors [128]. SnO_2 and WO_x have a long history for sensing applications, especially in gas sensing [129].

3.4 Hydrogen fuel production

The conversion of solar energy into hydrogen represents an attractive and challenging alternative for photovoltaic solar cells. In 1972, a crucial discovery in the field of photocatalysis was done by Honda and Fujishima explaining the Honda–Fujishima effect which shows the electrolysis of water and the evolution of the hydrogen gas [103]. Since then, many nanomaterials have been seen which act as a photocatalyst to produce hydrogen fuel by inducing photocatalysis in water. Process for H_2 evolution by a photocatalyst in presence of the sacrificial reagents is shown in Fig. 15, photogenerated holes irreversibly oxidize the sacrificial reagents instead of water making the photocatalyst electron-rich thus increasing the H_2 evolution process.

Several metal oxide semiconductors were used to split water into hydrogen and oxygen upon illumination. The most straightforward method to produce hydrogen from water and sunlight is by coupling an electrolyzer to a solar cell array. TiO_2 and SnO_2 possess high chemical stability over a broad range of pH and applied potentials; however under light illumination the decay of ZnO was observed [131]. WO_3 and other metal oxide semiconductors such as iron oxide (Fe_2O_3) have also been studied extensively for the use of photoanodes [132, 133].

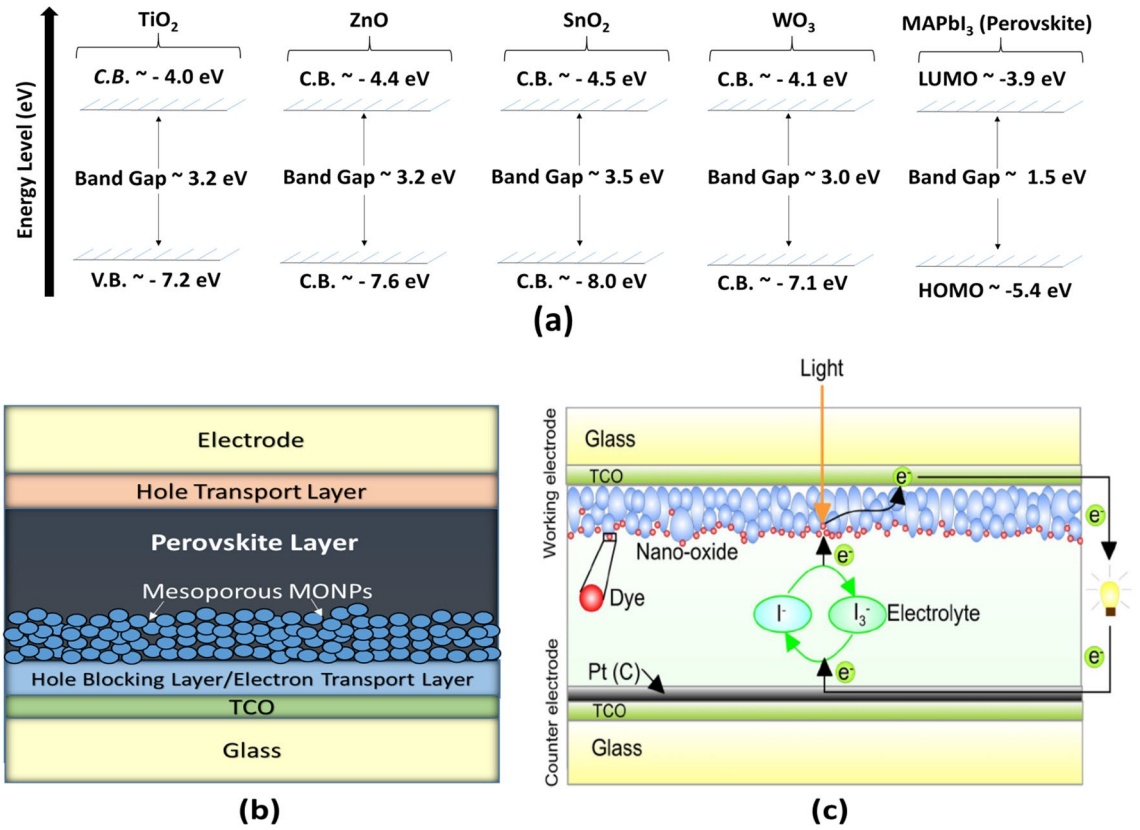

Fig. 13 Conduction band minimum and valence band maximum of TiO_2, ZnO, SnO_2 and WO_3 along with the typical HOMO–LUMO levels of methylammonium lead iodide ($MAPbI_3$) perovskite (**a**) [113–115], MONPs as electron transport layer and mesoporous scaffolds in perovskite solar cell (**b**) and in dye sensitized solar cell (**c**) [116]

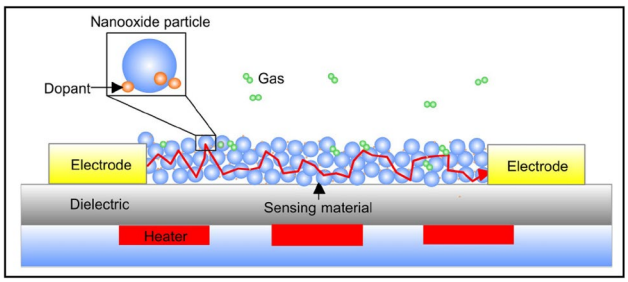

Fig. 14 Schematic representation of gas sensing device and sensing principle [116]

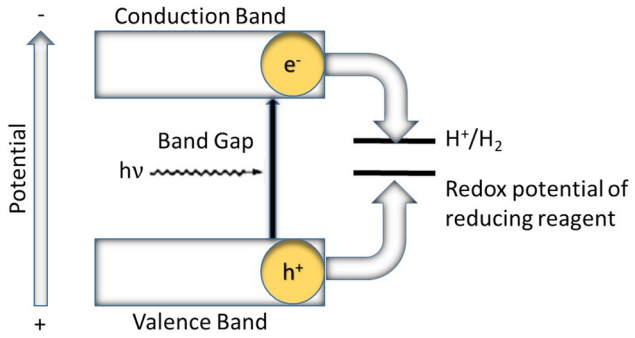

Fig. 15 Photocatalytic H_2 evolution in the presence of a reducing agent [130]

3.5 Biomedical applications

Metal oxides owning special electrical, optical, and magnetic properties are promising for healthcare and medical applications like cosmetics, self-cleaning coatings, biosensors, bio-separation, antibacterial, and drug delivery [134]. MONPs are widely used in tissue engineering for creating biological alternatives of tissues and organs in mammals (Fig. 16). MONPs porous scaffolds can guide the cell growth and tissue regeneration in scaffold by the formation of reactive oxygen species such as O_2^- and H_2O_2 which can be helpful in cell function, adhesion, proliferation, angiogenesis and wound healing [135].

In few studies, different MONPs have been studied like TiO_2 nanocoral architecture that provides a highly controllable drug release system under UV light for cancer chemotherapy [136]. ZnO nanostructures show superior antibacterial, anticancer, biosensor, bioimaging,

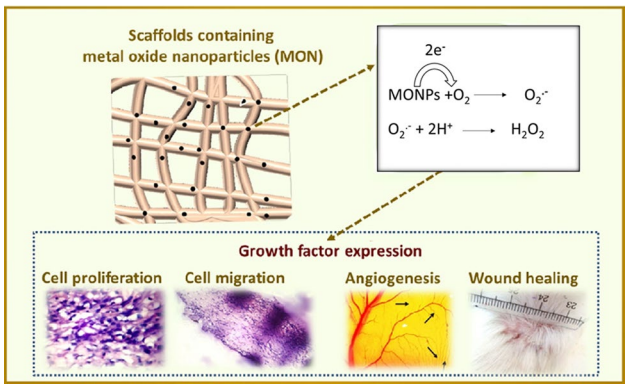

Fig. 16 Scheme showing the role of MONPs in tissue engineering scaffolds [135]

antimicrobial, and excellent UV-blocking properties [137, 138]. SnO_2 NPs can be used for its antibacterial properties [83]. WO_3–SnO_2 sensor is used in non-invasive detection of human breath analysis [139]. Tungsten oxide NPs can be a good alternative material for electrochemical non-mediated biosensors [140]. Hybridized tungsten oxide nanostructures are also used for food quality assessment as a dye detector [141].

3.6 Energy storage applications

Supercapacitors are center of attention for their use as an energy storage device. The charge storage mechanism of a supercapacitor strongly depends on the surface properties of the electrode materials. These nanomaterials possess high surface area along with high surface energy, but the aggregation of nanoparticles is the most challenging problem. To overcome this problem mesoporous nanomaterials are widely used for electrode fabrication of supercapacitors. Mesoporous nanomaterials such as composites of metal oxides of TiO_2 and V_2O_5 (vanadium pentaoxide) are employed as electrode material for the supercapacitor due to their excellent physical properties [142]. Various studies are reported for MONPs based electrodes in supercapacitors. For example, Sasirekha et al. [143] synthesized ZnO NPs via sol–gel method, coated with carbon (ZnO/C) to prepare an electrode for supercapacitor, exhibiting a specific capacitance of 92 F/g. Similarly, Bonu et al. [144] and He et al. [145] studied the role of SnO_2 quantum dots and SnO_2 NPs embedded in carbon microspheres which showed the specific capacitance as high as 420 F/g.

3.7 Artificial photosynthesis

Artificial photosynthesis is a chemical process that mimics the natural process of photosynthesis, a process that converts sunlight energy, CO_2 and water to fuel. An artificial photosynthetic system that directly produces fuels from sunlight could provide an approach to scalable energy storage and a technology for the carbon–neutral production of high-energy–density transportation fuels [146]. Various doped and undoped photoelectrodes have been explored by researchers to create such system using metal oxides nanostructures such as TiO_2, WO_3, Fe_2O_3 and Cu_2O [147–150]. Although these metal oxides make stable photoanodes, but their large bandgaps can only absorb very limited portion of the sunlight. However, there are some other inorganic semiconductors such as Si, CdTe, InP etc. which can also do the same task with an ultrathin protective layer of metal oxide which is nonporous, catalytic and have appropriate interfacial energetics. TiO_2 and NiO_x have shown ideal protection for the photoanodes as reported in some studies [151–153].

4 Future perspectives

The focus of research for creating novel materials is shifting nowadays towards size reduction due to which MONPs are paving their way in different industrial applications like electronics, drug delivery tools, sensors, solar energy etc. Currently, it is a global demand to change the approach for electrical energy production from burning fossil fuels to some form of a renewable energy source to fix serious environmental concerns like climate change and global warming. Utilizing the energy received from sun is by far one of the most explored form of renewable energy which ultimately gave rise to the field of photovoltaics. The synthesis of different nanostructures like nanorods, nanospheres, nanotubes, nanofibers, nanosheets etc. having different dimensionality and porosity has demonstrated their role in evolution of electronic devices especially in solution processed solar cells for achieving breakthrough efficiencies. A hunt for creating novel materials by a simple and cost-effective sol–gel processing can be helpful to execute powerful ideas to advance the nanoscale photovoltaic technology to the next level which can help in solving the energy crisis globally. For the production of different nanostructures with desired specific properties, the reaction parameters such as pH, reaction time, temperature, pressure during synthesis can be tuned to achieve novel nanostructures. Also, beside their useful applications it is important to keep an eye on minimizing the environmental hazards which can arise due to by-products of the reactions and by MONPs itself.

5 Conclusion

In conclusion, we have summarized the reported sol–gel synthesis route for different metal oxide nanoparticles (MONPs). The various processing steps involved in

sol–gel synthesis are systematically elaborated. Sol–gel synthesis route has shown various advantages over other physical and chemical synthesis procedures due to ambient temperature processing, good control over texture of the produced NPs, faster process and economically less expensive. Sol–gel procedures to synthesize particularly TiO_2, ZnO, SnO_2 and WO_3 MONPs are discussed along with a brief summary of the materials characterization to study the crystal structure, morphology, optical properties, bandgap, elemental composition, shape, size etc. Also, the role of MONPs involved in the different applications such as photocatalysis, photovoltaics, hydrogen production, gas sensors, biomedical, artificial photosynthesis, and energy storage is discussed. We think, scientific discussion and summarized data provided in this review will be helpful for the researchers around the world working on MONPs and their applications.

Acknowledgements The authors acknowledge the researchers from Gautam Buddha University, Greater Noida, UP, India and Dongguk University, Seoul, South Korea for fruitful discussion.

Author contributions All authors contributed to the manuscript. All authors read and approved the final manuscript.

Funding Not applicable.

Compliance with ethical standards

Conflict of interest The author declares no competing interests.

References

1. X. Chen, A. Selloni, Chem. Rev. **114**, 9281–9282 (2014)
2. S. Akin, S. Sonmezoglu, Chapter 2—metal oxide nanoparticles as electron transport layer for highly efficient dye-sensitized solar cells, in *Emerging materials for energy conversion and storage*, ed. by K.Y. Cheong, G. Impellizzeri, M.A. Fraga (Elsevier, Amsterdam, 2018), pp. 39–79
3. B.G. Rao, D. Mukherjee, B.M. Reddy, Chapter 1—novel approaches for preparation of nanoparticles, in *Nanostructures for novel therapy*, ed. by D. Ficai, A.M. Grumezescu (Elsevier, Amsterdam, 2017), pp. 1–36
4. B.R. Cuenya, Thin Solid Films **518**, 3127–3150 (2010)
5. M. Haruta, J. New. Mat. Electrochem. Syst. **7**, 163–172 (2004)
6. N. Tian, Z.-Y. Zhou, S.-G. Sun, Y. Ding, Z.L. Wang, Science **316**, 732–735 (2007)
7. R. Xu, D. Wang, J. Zhang, Y. Li, Chemistry **1**, 888–893 (2006)
8. I.A. Rahman, V. Padavettan, J. Nanomater. **2012**, 15 (2012)
9. F. Adam, C. Thiam-Seng, J. Andas, J. Sol-Gel. Sci. Technol. **59**, 580–583 (2011)
10. M. Catauro, E. Tranquillo, G. Dal Poggetto, M. Pasquali, A. Dell'Era, S. Ciprioti, Materials **11**, 2364 (2018)
11. S.M. Gupta, M. Tripathi, Cent. Eur. J. Chem. **10**, 279–294 (2012)
12. B.E. Yoldas, J. Mater. Sci. **14**, 1843–1849 (1979)
13. G.W. Scherer, J. Non-Cryst. Solids **100**, 77–92 (1988)
14. S.L. Isley, R.L. Penn, J. Phys. Chem. C **112**, 4469–4474 (2008)
15. C. de Coelho Escobar, J.H.Z. dos Santos, J. Sep. Sci. **37**, 868–875 (2014)
16. K. Kajihara, J. Asian Ceram. Soc. **1**, 121–133 (2013)
17. L.L. Hench, J.K. West, Chem. Rev. **90**, 33–72 (1990)
18. M. Niederberger, N. Pinna, *Metal oxide nanoparticles in organic solvents: synthesis, formation, assembly and application* (Springer, New York, 2009)
19. M.M. Collinson, H. Wang, R. Makote, A. Khramov, J. Electroanal. Chem. **519**, 65–71 (2002)
20. T. White, Y. Li, S.H. Lim, Rev. Adv. Mater. Sci. **5**, 211–215 (2003)
21. B. Li, X. Wang, M. Yan, L. Li, Mater. Chem. Phys. **78**, 184–188 (2003)
22. R. Vijayalakshmi, V. Rajendran, Synthesis and characterization of nano-TiO_2 via different methods. Arch. Appl. Sci. Res. **4**, 1183–1190 (2012)
23. W. Jaroenworaluck, N. Sunsaneeyametha, R. Kosachan, Stevens. Surf. Interface Anal. **38**, 473–477 (2006)
24. R. Verma, B. Mantri, A.K.S. Ramphal, Adv. Mater. Lett. **6**, 324–333 (2015)
25. R. Verma, A. Awasthi, P. Singh, R. Srivastava, H. Sheng, J. Wen, D.J. Miller, A.K. Srivastava, J. Colloid Interface Sci. **475**, 82–95 (2016)
26. H. Li, Z. Bian, J. Zhu, D. Zhang, G. Li, Y. Huo, H. Li, Y. Lu, J. Am. Chem. Soc. **129**, 8406–8407 (2007)
27. T.A. Kandiel, L. Robben, A. Alkaim, D. Bahnemann, Photochem. Photobiol. Sci. **12**, 602–609 (2013)
28. L. Zhang, V.M. Menendez-Flores, N. Murakami, T. Ohno, Appl. Surf. Sci. **258**, 5803–5809 (2012)
29. D. Sarkar, C.K. Ghosh, K.K. Chattopadhyay, CrystEngComm **14**, 2683–2690 (2012)
30. H. Bai, Z. Liu, D.D. Sun, J. Mater. Chem. **22**, 18801–18807 (2012)
31. D. Reyes-Coronado, G. Rodríguez-Gattorno, M. Espinosa-Pesqueira, C. Cab, R.D. de Coss, G. Oskam, Nanotechnology **19**, 145605 (2008)
32. R. Verma, J. Gangwar, A.K. Srivastava, RSC Adv. **7**, 44199–44224 (2017)
33. B. Singh, Birajdar. RSC Adv. **7**, 54053–54062 (2017)
34. G.W. Simmons, B.C. Beard, J. Phys. Chem. **91**, 1143–1148 (1987)
35. C. Su, L. Liu, M. Zhang, Y. Zhang, C. Shao, CrystEngComm **14**, 3989–3999 (2012)
36. M. Mahlambi, A. Mishra, S.B. Mishra, R. Krause, B. Mamba, A. Raichur, Comparison of rhodamine B degradation under UV irradiation by two phases of titania nano-photocatalyst. J. Thermal Anal. Calorim. **110**(2), 847–855 (2011)
37. Y.-H. Shih, C.-H. Lin, Environ. Sci. Pollut. Res. **19**, 1652–1658 (2012)
38. Ö. Kerkez, E. Kibar, K. Dayıoğlu, F. Gedik, A. Akin, A.P.Ş. Özkara-Aydınoğlu, A comparative study for removal of different dyes over M/TiO2 (M = Cu, Ni, Co, Fe, Mn and Cr) photocatalysts under visible light irradiation. J. Photochem. Photobiol. A **311**, 176–185 (2015)
39. S. Yadav, G. Jaiswar, J. Chin. Chem. Soc. **64**, 103–116 (2017)
40. P. Peerakiatkhajohn, W. Onreabroy, C. Chawengkijwanich, S. Chiarakorn, Preparation of visible-light-responsive TiO2 doped Ag thin film on PET plastic for BTEX treatment. J. Sustain. Energy Environ. **2**, 121–125 (2011)
41. H. Pan, X.D. Wang, S.S. Xiao, L.G. Yu, Z.J. Zhang, Preparation and characterization of TiO2 nanoparticles surface-modified by octadecyltrimethoxysilane. Indian J. Eng. Mater. Sci. **20**(6), 561–567 (2013)
42. B.B. Lakshmi, P.K. Dorhout, C.R. Martin, Chem. Mater. **9**, 857–862 (1997)

43. Z. Wang, L. Shi, F. Wu, S. Yuan, Y. Zhao, M. Zhang, Nanotechnology **22**, 275502 (2011)
44. X.-G. Hou, M.-D. Huang, X.-L. Wu, A.-D. Liu, Chem. Eng. J. **146**, 42–48 (2009)
45. R. Dubey, Mater. Lett. **215**, 312–317 (2018)
46. A.O. Araoyinbo, M.M.A.B. Abdullah, M.A.A.M. Salleh, N.N.A. Aziz, A.I. Azmi, *IOP Conference Series: Materials Science and Engineering* (IOP Publishing, Bristol, 2018), p. 012011
47. T.H. Mahato, G.K. Prasad, B. Singh, J. Acharya, A.R. Srivastava, R. Vijayaraghavan, J. Hazard. Mater. **165**, 928–932 (2009)
48. C. Hariharan, Appl. Catal. A **304**, 55–61 (2006)
49. M. Ristić, S. Musić, M. Ivanda, S. Popović, J. Alloy. Compd. **397**, L1–L4 (2005)
50. S. Yue, Z. Yan, Y. Shi, G. Ran, Mater. Lett. **98**, 246–249 (2013)
51. V. Mayekar, S. Dhar, Radha, To study the role of temperature and sodium hydroxide concentration in the synthesis of zinc oxide nanoparticles. J. Sci. Res. Publ. **3**(11), 2250–3153 (2013)
52. S. Zavar, Arab. J. Chem. **10**, S67–S70 (2017)
53. N. Hassan, M. Hashim, M. Bououdina, Ceram. Int. **39**, 7439–7444 (2013)
54. D. Ju, H. Xu, J. Zhang, J. Guo, B. Cao, Sensors Actuators B **201**, 444–451 (2014)
55. S. Yue, J. Lu, J. Zhang, Mater. Chem. Phys. **117**, 4–8 (2009)
56. N. Sagasti, D. Bouropoulos, A. Kouzoudis, E. Panagiotopoulos, J. Topoglidis, Gutiérrez. Materials **10**, 849 (2017)
57. P. Samanta, A. Saha, T. Kamilya, (2014)
58. Y. Zhang, E. Xie, Appl. Phys. A **99**, 955–960 (2010)
59. M. Navaneethan, G.K. Mani, S. Ponnusamy, K. Tsuchiya, C. Muthamizhchelvan, S. Kawasaki, Y. Hayakawa, J. Alloy. Compd. **698**, 555–564 (2017)
60. J.T. Chen, J. Wang, R.F. Zhuo, D. Yan, J. Feng, F. Zhang, P. Yan, Appl. Surf. Sci. **255**, 3959–3964 (2009)
61. J. Wang, Y. Li, Y. Kong, J. Zhou, J. Wu, X. Wu, W. Qin, Z. Jiao, L. Jiang, RSC Adv. **5**, 81024–81029 (2015)
62. S.S. Shinde, P.S. Shinde, Y.W. Oh, D. Haranath, C.H. Bhosale, K.Y. Rajpure, Appl. Surf. Sci. **258**, 9969–9976 (2012)
63. S.K. Patil, S.S. Shinde, K.Y. Rajpure, Ceram. Int. **39**, 3901–3907 (2013)
64. S.S. Shinde, A.P. Korade, C.H. Bhosale, K.Y. Rajpure, J. Alloy. Compd. **551**, 688–693 (2013)
65. S.S. Shinde, P.S. Patil, R.S. Gaikwad, R.S. Mane, B.N. Pawar, K.Y. Rajpure, J. Alloy. Compd. **503**, 416–421 (2010)
66. M.A. Mahadik, S.S. Shinde, Y.M. Hunge, V.S. Mohite, S.S. Kumbhar, A.V. Moholkar, K.Y. Rajpure, C.H. Bhosale, J. Alloy. Compd. **611**, 446–451 (2014)
67. S.S. Shinde, P.S. Shinde, C.H. Bhosale, K.Y. Rajpure, J. Phys. D **41**, 105109 (2008)
68. S.S. Shinde, C.H. Bhosale, K.Y. Rajpure, J. Photochem. Photobiol. B **113**, 70–77 (2012)
69. S.S. Shinde, C.H. Bhosale, K.Y. Rajpure, J. Photochem. Photobiol. B **120**, 1–9 (2013)
70. S.S. Shinde, P.S. Shinde, C.H. Bhosale, K.Y. Rajpure, J. Photochem. Photobiol. B **104**, 425–433 (2011)
71. S.S. Shinde, K.Y. Rajpure, Mater. Res. Bull. **46**, 1734–1737 (2011)
72. R. Ullah, J. Dutta, J. Hazard. Mater. **156**, 194–200 (2008)
73. S.C. Hossain, Y. Ghosh, C. Boontongkong, J.Dutta Thanachayanont, Growth of zinc oxide nanowires and nanobelts for gas sensing applications. J. Metastab. Nanocryst. Mater. **23**, 27–30 (2005)
74. Y. Natsume, H. Sakata, Thin Solid Films **372**, 30–36 (2000)
75. T. Nagase, T. Ooie, J. Sakakibara, Thin Solid Films **357**, 151–158 (1999)
76. F. Gu, S. Fen Wang, C. Feng Song, M. Kai Lü, Y. Xin Qi, G. Jun Zhou, D. Xu, D. Rong Yuan, Chem. Phys. Lett. **372**, 451–454 (2003)
77. R. Adnan, N.A. Razana, I.A. Rahman, M.A. Farrukh, J. Chin. Chem. Soc. **57**, 222–229 (2010)
78. J. Zhang, L. Gao, J. Solid State Chem. **177**, 1425–1430 (2004)
79. S. de Monredon, A. Cellot, F. Ribot, C. Sanchez, L. Armelao, L. Gueneau, L. Delattre, J. Mater. Chem. **12**, 2396–2400 (2002)
80. M. Ristić, S. Ivanda, S. Popović, S. Musić, J. Non-Cryst. Solids **303**, 270–280 (2002)
81. M. Aziz, S.S. Abbas, W.R. Baharom, Mater. Lett. **91**, 31–34 (2013)
82. S. Gnanam, V. Rajendran, J. Sol-Gel. Sci. Technol. **53**, 555–559 (2010)
83. M.N. Al-Hada, M.H. Kamari, A.A. Baqer, H.A. Shaari, E. Saion, Nanomaterials **8**, 250 (2018)
84. F. Li, J. Song, H. Yang, S. Gan, Q. Zhang, D. Han, A. Ivaska, L. Niu, Nanotechnology **20**, 455602 (2009)
85. Z. Wang, H.A. Al-Jawhari, P.K. Nayak, J. Caraveo-Frescas, N. Wei, M.N. Hedhili, H.N. Alshareef, Sci. Rep. **5**, 9617 (2015)
86. T. Moon, S.-T. Hwang, D.-R. Jung, D. Son, C. Kim, J. Kim, M. Kang, B. Park, J. Phys. Chem. C **111**, 4164–4167 (2007)
87. S. Stankovich, R.D. Piner, X. Chen, N. Wu, S.T. Nguyen, R.S. Ruoff, J. Mater. Chem. **16**, 155–158 (2006)
88. S. Das, D.-Y. Kim, C.-M. Choi, Y.B. Hahn, J. Cryst. Growth **314**, 171–179 (2011)
89. J.C. Bessière, M.C. Badot, J. Certiat, V. Livage, N. Lucas, Baffier. Electrochim. Acta **46**, 2251–2256 (2001)
90. M. Breedon, P. Spizzirri, M. Taylor, J. du Plessis, D. McCulloch, J. Zhu, L. Yu, Z. Hu, C. Rix, W. Wlodarski, K. Kalantar-zadeh, Cryst. Growth Des. **10**, 430–439 (2010)
91. X.Z. Li, F.B. Li, C.L. Yang, W.K. Ge, J. Photochem. Photobiol. A **141**, 209–217 (2001)
92. J. Shi, G. Hu, Y. Sun, M. Geng, J. Wu, Y. Liu, M. Ge, J. Tao, M. Cao, N. Dai, Sensors Actuators B **156**, 820–824 (2011)
93. D. Susanti, A.A.G.P. Diputra, L. Tananta, H. Purwaningsih, G.E. Kusuma, C. Wang, S. Shih, Y. Huang, Front. Chem. Sci. Eng. **8**, 179–187 (2014)
94. C. Santato, M. Odziemkowski, M. Ulmann, J. Augustynski, J. Am. Chem. Soc. **123**, 10639–10649 (2001)
95. X. Duan, S. Xiao, L. Wang, H. Huang, Y. Liu, Q. Li, T. Wang, Nanoscale **7**, 2230–2234 (2015)
96. C. Chacón, M. Rodríguez-Pérez, G. Oskam, G. Rodríguez-Gattorno, J. Mater. Sci. **26**, 5526–5531 (2015)
97. L. Wang, H. Hu, J. Xu, S. Zhu, A. Ding, C. Deng, Journal of Materials Research, (2019) 1-9
98. A. Shpak, M. Korduban, V. Medvedskij, Kandyba. J. Electron Spectrosc. Relat. Phenom. **156**, 172–175 (2007)
99. T. He, Y. Ma, Y. Cao, X. Hu, H. Liu, G. Zhang, W. Yang, J. Yao, J. Phys. Chem. B **106**, 12670–12676 (2002)
100. I. Benoit, Y.C. Paramasivam, P. Nah, P. Roy, Schmuki. Electrochem. Commun. **11**, 728–732 (2009)
101. L. Wang, A. Teleki, S.E. Pratsinis, P.I. Gouma, Chem. Mater. **20**, 4794–4796 (2008)
102. C.B. Ong, L.Y. Ng, A.W. Mohammad, Renew. Sustain. Energy Rev. **81**, 536–551 (2018)
103. X. Chen, S.S. Mao, Chem. Rev. **107**, 2891–2959 (2007)
104. M.M. Khan, S.F. Adil, A. Al-Mayouf, J. Saudi Chem. Soc. **19**, 462–464 (2015)
105. K. Mondal, A. Sharma, RSC Adv. **6**, 83589–83612 (2016)
106. H.M. Yadav, J.-S. Kim, S.H. Pawar, Korean J. Chem. Eng. **33**, 1989–1998 (2016)
107. R. Khanom, S. Parveen, M. Hasan, Am. Sci. Res. J. Eng. Technol. Sci. **46**, 111–121 (2018)
108. K. Gold, B. Slay, M. Knackstedt, A.K. Gaharwar, Adv. Therap. **1**, 1700033 (2018)

109. G. Duan, L. Chen, Z. Jing, P. De Luna, L. Wen, L. Zhang, L. Zhao, J. Xu, Z. Li, Z. Yang, R. Zhou, Chem. Res. Toxicol. **32**, 1357–1366 (2019)
110. A. Perez-Tomas, D. Mingorance, M. Tanenbaum, *Lira-Cantu, Metal Oxides in Photovoltaics: All-Oxide, Ferroic, and Perovskite Solar Cells* (Elsevier, Amsterdam, 2017)
111. R. Singh, I. Ryu, H. Yadav, J. Park, J.W. Jo, S. Yim, J.-J. Lee, Sol. Energy **185**, 307–314 (2019)
112. H. Xie, X. Yin, P. Chen, J. Liu, C. Yang, W. Que, G. Wang, Mater. Lett. **234**, 311–314 (2019)
113. C.-C. Chueh, C.-Z. Li, A.K.-Y. Jen, Energy Environ. Sci. **8**, 1160–1189 (2015)
114. H.P. Hussain, J. Tran, J. Jaksik, N. Moore, M.J. Islam, Uddin Emerg. Mater. **1**, 133–154 (2018)
115. T. Gershon, Mater. Sci. Technol. **27**, 1357–1371 (2011)
116. M.S. Chavali, M.P. Nikolova, SN Appl. Sci. **1**, 607 (2019)
117. J. Wei, G. Ji, C. Zhang, L. Yan, Q. Luo, C. Wang, Q. Chen, J. Yang, L. Chen, C.-Q. Ma, ACS Nano **12**, 5518–5529 (2018)
118. Z. Zheng, S. Zhang, J. Wang, J. Zhang, D. Zhang, Y. Zhang, Z. Wei, Z. Tang, J. Hou, H. Zhou, J. Mater. Chem. A **7**, 3570–3576 (2019)
119. K. Al-Attafi, A. Nattestad, Y. Yamauchi, S.X. Dou, J.H. Kim, Sci. Rep. **7**, 10341 (2017)
120. K. Mahmood, S. Sarwar, M.T. Mehran, RSC Adv. **7**, 17044–17062 (2017)
121. H.S. Jung, N.G. Park, Small **11**, 10–25 (2015)
122. B. Tan, Y. Wu, J. Phys. Chem. B **110**, 15932–15938 (2006)
123. D. Liu, T.L. Kelly, Nat. Photon. **8**, 133 (2014)
124. Y. Li, J. Zhu, Y. Huang, F. Liu, M. Lv, S. Chen, L. Hu, J. Tang, J. Yao, S. Dai, RSC Adv. **5**, 28424–28429 (2015)
125. K. Mahmood, B.S. Swain, A.R. Kirmani, A. Amassian, J. Mater. Chem. A **3**, 9051–9057 (2015)
126. Materials Dey, Sci. Eng. B **229**, 206–217 (2018)
127. C. Wang, L. Yin, L. Zhang, D. Xiang, R. Gao, Sensors **10**, 2088–2106 (2010)
128. H. Meixner, U. Lampe, Sensors Actuators B **33**, 198–202 (1996)
129. H. Zheng, J.Z. Ou, M.S. Strano, R.B. Kaner, A. Mitchell, K. Kalantar-zadeh, Adv. Func. Mater. **21**, 2175–2196 (2011)
130. Y. Kudo, Miseki. Chem. Soc. Rev. **38**, 253–278 (2009)
131. R. van de Krol, Y. Liang, J. Schoonman, J. Mater. Chem. **18**, 2311–2320 (2008)
132. C. Jorand Sartoretti, B.D. Alexander, R. Solarska, I.A. Rutkowska, J. Augustynski, R. Cerny, J. Phys. Chem. B **109**, 13685–13692 (2005)
133. C. Santato, M. Ulmann, J. Augustynski, J. Phys. Chem. B **105**, 936–940 (2001)
134. Z. Sadowski, A. Pawlowska, Synthesis of Metal Oxide Nanoparticles and Its Biomedical Applications, in *Nanotechnology Applied To Pharmaceutical Technology*, ed. by M. Rai, C. Alves dos Santos (Springer International Publishing, Cham, 2017), pp. 91–111
135. R. Augustine, A.P. Mathew, A. Sosnik, Appl. Mater. Today **7**, 91–103 (2017)
136. H.M. Yadav, N.D. Thorat, M.M. Yallapu, S.A.M. Tofail, J.-S. Kim, J. Mater. Chem. B **5**, 1461–1470 (2017)
137. J. Jiang, J. Pi, J. Cai, The advancing of zinc oxide nanoparticles for biomedical applications. Bioinorg. Chem. Appl. (2018). https://doi.org/10.1155/2018/1062562
138. Y. Zhang, T.R. Nayak, H. Hong, W. Cai, Curr. Mol. Med. **13**, 1633–1645 (2013)
139. A.K. Nayak, R. Ghosh, S. Santra, P.K. Guha, D. Pradhan, Nanoscale **7**, 12460–12473 (2015)
140. L. Santos, C.M. Silveira, E. Elangovan, J.P. Neto, D. Nunes, L. Pereira, R. Martins, J. Viegas, J.J.G. Moura, S. Todorovic, M.G. Almeida, E. Fortunato, Sensors Actuators B **223**, 186–194 (2016)
141. P. Kumar, P.K. Sarswat, M.L. Free, Sci. Rep. **8**, 3348 (2018)
142. A. Ray, S. Roy, S. Saha, *Das, Transition Metal Oxide-Based Nano-materials for Energy Storage Application. Science Technology and Advanced Application of Supercapacitors* (INTECHOPEN, London, 2019)
143. S. Sasirekha, G. Arumugam, Muralidharan. Appl. Surf. Sci. **449**, 521–527 (2018)
144. V. Bonu, B. Gupta, S. Chandra, A. Das, S. Dhara, A.K. Tyagi, Electrochimica Acta **203**, 230–237 (2016)
145. C. He, Y. Xiao, H. Dong, Y. Liu, M. Zheng, K. Xiao, X. Liu, H. Zhang, B. Lei, Electrochim. Acta **142**, 157–166 (2014)
146. N.S. Lewis, Nat. Nanotechnol. **11**, 1010–1019 (2016)
147. Q. Zhang, X. Xu, S. Chen, G.B. Bodedla, M. Sun, Q. Hu, Q. Peng, B. Huang, H. Ke, F. Liu, T.P. Russell, Sustain. Energy Fuels **2**, 2616–2624 (2018)
148. X. Chen, L. Liu, P.Y. Yu, S.S. Mao, Science **331**, 746–750 (2011)
149. W. Cheng, J. He, Z. Sun, Y. Peng, T. Yao, Q. Liu, Y. Jiang, F. Hu, Z. Xie, B. He, S. Wei, J. Phys. Chem. C **116**, 24060–24067 (2012)
150. H. Qi, J. Wolfe, D. Fichou, Z. Chen, Sci. Rep. **6**, 30882 (2016)
151. Y.W. Chen, J.D. Prange, S. Dühnen, Y. Park, M. Gunji, C.E.D. Chidsey, P.C. McIntyre, Nat. Mater. **10**, 539–544 (2011)
152. A.G. Scheuermann, J.P. Lawrence, K.W. Kemp, T. Ito, A. Walsh, C.E.D. Chidsey, P.K. Hurley, P.C. McIntyre, Nat. Mater. **15**, 99–105 (2016)
153. K. Sun, M.T. McDowell, A.C. Nielander, S. Hu, M.R. Shaner, F. Yang, B.S. Brunschwig, N.S. Lewis, J. Phys. Chem. Lett. **6**, 592–598 (2015)